Manuscript prepared for Atmos. Chem. Phys. Discuss.
with version 2014/09/16 7.15 Copernicus papers of the LaTeX class copernicus.cls.
Date: 15 May 2015

The southern stratospheric gravity-wave hot spot: individual waves and their momentum fluxes measured by COSMIC GPS-RO

N. P. Hindley[1], **C. J. Wright**[1], **N. D. Smith**[1], **and N. J. Mitchell**[1]

[1]Centre for Space, Atmospheric and Oceanic Sciences, University Of Bath, BA2 7AY, UK

Correspondence to: Neil Hindley (n.hindley@bath.ac.uk)

Abstract

Nearly all general circulation models significantly fail to reproduce the observed behaviour of the Southern wintertime polar vortex. It has been suggested that these biases result from an under-estimation of gravity-wave drag on the atmosphere at latitudes near 60°S, especially around the "hot-spot" of intense gravity wave fluxes above the mountainous Southern Andes and Antarctic peninsula. Here, we use Global Positioning System (GPS) Radio Occultation (RO) data from the COSMIC satellite constellation to determine the properties of gravity waves in the hot-spot and beyond. We show considerable southward propagation to latitudes near 60°S of waves apparently generated by the southern Andes. We propose that this propagation may account for much of the wave drag missing from the models. Furthermore, there is a long leeward region of increased gravity-wave energy that sweeps eastwards from the mountains over the Southern Ocean. Despite its striking nature, the source of this region has historically proved difficult to determine. Our observations suggest that this region includes both waves generated locally and orographic waves advected downwind from the hot-spot. We describe and use a new wavelet analysis technique for the quantitative identification of individual waves from COSMIC temperature profiles. This analysis reveals different geographical regimes of wave amplitude and short-timescale variability in the wave field over the Southern Ocean. Finally, we use the large numbers of closely spaced pairs of profiles from the deployment phase of the COSMIC constellation in 2006 to make estimates of gravity-wave horizontal wavelengths. We show that, given sufficient observations, GPS-RO can produce physically reasonable estimates of stratospheric gravity wave momentum flux in the hot-spot, which are consistent with measurements made by other techniques. We discuss our results in the context of previous satellite and modelling studies to develop a better understanding of the nature and origins of waves in the southern stratosphere.

1 Introduction

Gravity waves are propagating mesoscale disturbances that transport energy and momentum in fluid environments. They are a vital component of the atmospheric system and a key driving mechanism in the middle and lower atmosphere through drag and diffusion processes (e.g. Fritts and Alexander, 2003, and citations therein). However, despite their importance, considerable uncertainty remains about gravity-wave sources, fluxes, propagation and variability.

A striking example of the importance of accurately assessing gravity-wave fluxes is that that nearly all global climate models (GCMs) have a systematic bias in their representation of the southern stratosphere. In particular, in the models the break down of the winter polar vortex occurs too late in the year, the polar vortex winds are too strong and the polar vortex temperatures are too low. This "cold-pole" bias is a long-standing problem and has been identified as a serious impediment to model progress, leading to discrepancies in properties including simulated Antarctic ozone trends and southern-hemisphere climate (e.g. McLandress et al., 2012). These problems are believed to arise because the models are deficient in gravity-wave drag in the stratosphere at latitudes near 60S. This deficiency may arise because in the real atmosphere waves from other latitudes propagate into this latitude belt, or because the sources of gravity waves in the models under-represent the in situ generation of waves. Determining the nature of gravity waves at latitudes near 60S is thus a significant problem.

During austral winter, observations have revealed the southern hemisphere stratosphere to be home to some of the most intense gravity wave activity on Earth. At high southern latitudes, the mountains of the southern Andes and Antarctic Peninsula are a hot spot of stratospheric gravity wave momentum flux (e.g. Eckermann and Preusse, 1999; Ern et al., 2004; Alexander and Teitelbaum, 2007; Alexander et al., 2008; Alexander and Teitelbaum, 2011). Several second-order hot spots include South Georgia (Alexander et al., 2009) and other small islands in and around the Southern Ocean (Alexander and Grimsdell, 2013; Hoffmann et al., 2013). Accompanying the momentum flux hot spot is a long leeward distribution of increased gravity wave energy stretching eastwards from the southern Andes, Drake Passage and Antarctic Peninsula far over the Southern Ocean. This feature has puzzled researchers since it was first seen in spaceborne observations. Despite more than a decade of close observation (e.g. Wu and Waters, 1996; Wu and Jiang, 2002; Ern et al., 2004; Hei et al., 2008; Alexander et al., 2008, 2009; Yan et al., 2010; Gong et al., 2012; Hendricks et al., 2014; Preusse et al., 2014) its origins are still not incontestably understood.

It has been suggested that gravity waves in this region may have a number of orographic and non-orographic sources, such as the leeward propagation of mountain waves from the southern tip of South America and/or the northern tip of the Antarctic Peninsula (Preusse et al., 2002; Sato et al., 2009, 2012), baroclinic instabilities from tropospheric storm systems (Hendricks et al., 2014; Preusse et al., 2014) or spontaneous adjustment arising independently from, or as a result of, either or both of these primary processes. It is likely that the gravity waves observed in this region are a result of some or all of these processes overlapping in spatial and temporal regions.

However, quantitatively identifying and describing the location, magnitude and short-timescale variability of each gravity wave source through close observation has proved exceptionally challenging. It is perhaps for this reason that the current generation of General Circulation Models (GCMs) exhibit strong disagreement in the magnitude and distribution of the flux of horizontal psuedomomentum (hereafter referred to as momentum flux) due to gravity waves in the southern hemisphere stratosphere during austral winter compared to observations (Geller et al., 2013). Particularly large discrepancies are found over the mountains of the southern Andes and Antarctic Peninsula suggesting even orographic wave drag is not simulated consistently.

For the majority of operational GCMs used in numerical weather prediction (NWP), many gravity waves are sub-gridscale phenomena and their effects must be parametrized. Parametrizations vary greatly between GCMs, but tuning parameters may for example be chosen in order to produce comparable monthly-mean zonal-mean wind fields to observations (Geller et al., 2013) or obtain a realistic quasi-biennial oscillation (QBO) (e.g. Scaife et al., 2000) while remaining physically plausible. However, a current scarcity of robust observations of key gravity wave parameters means that these parametrizations are poorly constrained

(Alexander et al., 2010). With the advent of increased computing power in recent years, high spatial resolution GCMs without the need for gravity-wave parametrizations are becoming available (e.g. Watanabe et al., 2008). Such high-resolution modelling studies are promising (e.g. Sato et al., 2012), but discrepancies between observed and modelled parameters still remain. An in-depth review of the current state of gravity-wave modelling is presented by Preusse et al. (2014).

All of the above factors highlight the need for accurate measurements of gravity-wave sources, energies, fluxes and variability. Here, we use Global Positioning System radio occultation (GPS-RO) data to investigate the nature and origins of waves in the southern stratospheric gravity wave hot spot and associated leeward distribution of enhanced gravity wave energy. In Section 2, we present maps and cross-sections of gravity wave energy in the southern hemisphere, with implications for oblique focussing and leeward propagation of gravity waves into the southern stratospheric jet. In Section 3, we propose a new method for the quantitative identification of individual waves from GPS-RO profiles. We use this method to investigate the geographical distribution of wave amplitudes and short-timescale variability of individual gravity waves in the wave field over the Southern Ocean. In Section 4, we present a method for the estimation of gravity wave momentum flux from GPS-RO measurements over the southern Andes and Antarctic Peninsula using pairs of closely spaced and closely timed profiles. Our results are discussed in the context of other studies in Section 5, and in Section 6 the key results of the present study are summarised.

1.1 COSMIC GPS Radio Occultation

Launched in April 2006, The Constellation Observing System for Meteorology, Ionosphere and Climate (COSMIC) mission consists of six low Earth orbit ($\sim$800 km) satellites at $\sim$72° inclination and 30° separation. A detailed description of the COSMIC constellation and the radio occultation process is provided by Liou et al. (2007). Each satellite tracks occulting GPS satellites as they rise above or set below the Earth's horizon. As the GPS signal traverses the atmospheric limb, phase delay measurements attributable to changing vertical gradients of refractivity in the atmosphere are measured. Taking an integral along the line of sight, vertical profiles of dry temperature and pressure can be computed at the tangent point of the occultation via an Abel inversion (Fjeldbo et al., 1971). The dry temperature conversion breaks down in the presence of water vapour, but works well in the stratosphere, where water vapour is negligible. Kursinski et al. (1997) estimated a temperature retrieval accuracy of $\sim$0.3 K between 5-30 km, while Tsuda et al. (2011) verified multiple profiles with nearby radiosonde flights, returning discrepancies typically less than 0.5 K between 5-30 km.

In the present study we use COSMIC level 2 (version 2010.2640) post-processed dry temperature data from launch in April 2006 to the end of 2012. The sampling density of the COSMIC constellation in its final deployment configuration for a typical month in the southern hemisphere is shown in Figure 1. Good coverage at high latitudes and a band of preferential sampling at around 50°S as a result of orbital geometry means that COSMIC GPS-RO is well suited to a study of the southern gravity wave hot spot and the surrounding area.

1.1.1 Vertical and horizontal resolution limits

Currently, no single observational technique can study the entire gravity wave spectrum. Each technique is sensitive to a specific portion of the gravity wave spectrum, referred to as its observational filter (Alexander and Barnet, 2007; Preusse et al., 2008; Alexander et al., 2010).

The expected vertical and horizontal resolutions of GPS-RO are discussed at length by Kursinski et al. (1997). They showed that in the stratosphere, where reasonable spherical symmetry of the local atmosphere can be assumed, the vertical resolution ΔZ is primarily limited by Fresnel diffraction as

$$\Delta Z \approx 2(\lambda L_T)^{\frac{1}{2}} \approx 1.4\,\text{km} \tag{1}$$

where $\lambda = 19$ cm is the GPS L1 wavelength and $L_T \approx 28500$ km is the distance from the GPS satellite to the tangent point. The vertical resolution of GPS-RO improves significantly below the tropopause due to the exponential increase of refractivity gradient with decreasing altitude, but the combination of sharp vertical temperature gradient changes, increased humidity and smaller wave amplitudes make gravity wave study in this region difficult with GPS-RO via traditional methods.

Kursinski et al. (1997) showed that the horizontal line-of-sight resolution ΔL of GPS-RO could be defined as the horizontal distance travelled by the GPS ray as it enters and exits an atmospheric layer with vertical resolution ΔZ. By a first order geometric argument, ΔL and ΔZ are approximately related as

$$\Delta L = 2(2R\Delta Z)^{\frac{1}{2}} \tag{2}$$

where R is the radius of the atmosphere at the tangent point. The stratospheric horizontal line-of-sight resolution corresponding to a vertical resolution 1.4 km is ≈270 km. Gravity waves with $\lambda_H \lesssim 270$ km in the line of sight are hence less likely to be detected by GPS-RO. However, if the line of sight is not aligned with the wave's horizontal wavenumber vector, the projection of λ_H in the line of sight may be longer. This means that some waves with $\lambda_H < 270$ km may be resolved. As discussed by Alexander et al. (2009), orographic waves generated by the mountains of the southern Andes and Antarctic Peninsula may tend to have roughly westward orientated horizontal wavenumber vectors, and the majority of COSMIC occultations in this region tend to be preferentially aligned towards the north-south axis. As a result, the projection of λ_H in the COSMIC line of sight is longer and the likelihood of orographic wave detection over this region is increased.

The cross-beam horizontal resolution in the stratosphere is around 1.4 km, being only diffraction limited since horizontal refractivity gradients are generally small. This is of importance to our momentum flux study in section 4.

2 The gravity wave hot-spot and leeward region of increased E_p

In this section, we investigate the seasonal variability and distribution of potential energy per unit mass E_p in the southern hemisphere using COSMIC GPS-RO. E_p is a fundamental property of the gravity wave field and can provide a useful proxy for gravity wave activity.

In satellite observations, E_p is often derived from temperature perturbations around a background mean and can hence be calculated independently in each temperature profile. To calculate E_p, we first interpolate each dry temperature profile $T(z)$ to 100m resolution over the altitude range 0-50 km. We obtain a background temperature profile $T(\bar{z})$ by low-pass filtering $T(z)$ with a 2nd order Savitzky-Golay filter (Savitzky and Golay, 1964) with an 18 km frame-size and compute $T(z) - \bar{T}(z)$ to yield a temperature perturbation profile $T'(z)$.

Features with vertical scales less than ~2 km cannot be reliably disassociated with noise in GPS-RO temperature profiles (Marquardt and Healy, 2005), therefore we apply a 2nd order Savitzky-Golay low-pass filter with a 3 km frame size to suppress these small-scale features in $T'(z)$. Note that this step has virtually no effect on vertical wavelengths greater than ~4 km. The transmission functions for each step in our analysis is shown in Figure 6, and discussed further in Section 3.1. For the calculation of E_p in this section, only the blue and green dashed lines in Figure 6 apply.

This analysis provides a dynamic cut-off for vertical features in $T'(z)$. Features with vertical scales $\sim 3-14$ km are generally transmitted with a factor of at least 0.5, however transmission of vertical wavelengths longer than ~ 13 km (shorter than 4 km) decreases with increasing (decreasing) wavelength. It is important to note that no digital filter can provide a perfect cut-off in the frequency domain without introducing ringing artifacts into the spatial domain via the Gibbs phenomenon. We select the Savitzky-Golay filter as a reasonable trade-off between Gibbs ringing in the spatial domain and a sharp transition into the frequency stop band.

We use $T'(z)$ and $\bar{T}(z)$ to compute $E_p(z)$ as

$$E_p(z) = \frac{1}{2}\left(\frac{g}{N}\right)^2 \left(\frac{T'(z)}{\bar{T}(z)}\right)^2 \quad (3)$$

where g is acceleration due to gravity and N is the local Brunt-Väisälä frequency. It is not meaningful to take E_p at a single height z from a single profile since a full wave cycle does not exist (Alexander et al., 2008). Hence, E_p is often taken as an integral over a specified height interval when used as a proxy for gravity wave activity (e.g. Hei et al., 2008).

Unlike previous studies such as Alexander et al. (2009), no planetary wave removal techniques are applied to these data. At high latitudes, planetary waves typically have vertical scales much longer than 10 km, hence they are generally removed by our filtering method. We recognise however that some low-level planetary wave features may remain in the post-processed data.

2.1 Geographic distribution of E_p in the southern hemisphere

Figure 2 shows E_p in the southern hemisphere for each month in 2010 over the height interval 26-36 km. Note that this 10 km averaging window generally undersamples waves with $\lambda_Z > 10$ km.

We observe increased levels of E_p in austral winter and lower values in austral summer, consistent with other GPS-RO studies (e.g. Hei et al., 2008; Alexander et al., 2009). Between June and November, we see in Figure 2 a long leeward region of increased E_p stretching clockwise from the Southern Andes, Drake Passage and Antarctic Peninsula at around 70°W to around 180°E. This long leeward region of increased E_p is consistent with studies using other limb sounders such as the Upper Atmosphere Research Satellite Microwave Limb Sounder (UARS-MLS) (e.g. Wu and Waters, 1996), Cryogenic Infrared Spectrometers and Telescopes for the Atmosphere (CRISTA) (e.g. Ern et al., 2004) and the HIgh Resolution Dynamics Limb Sounder (HIRDLS) (e.g. Yan et al., 2010).

The magnitude and distribution of E_p in Figure 2 is also consistent with results from a high-resolution modelling study by Sato et al. (2012) using the T213L256 "Kanto" GCM developed by Watanabe et al. (2008). This is significant since Sato et al. used no gravity wave parametrizations, such that all resolved waves effects were spontaneously generated. They showed a long leeward distribution of E_p at 10 hPa ($\sim$31 km) stretching clockwise around the southern ocean from the southern Andes and Antarctic Peninsula to around 180°W during June-October. They proposed a downwind propagation mechanism for orographic waves from the mountains of the southern Andes and Antarctic Peninsula, whereby a wave could be freely advected by the component of the mean wind perpendicular to the wave's horizontal wavenumber vector, and primarily attributed the long leeward distribution to this mechanism.

Some differences in our observed distribution of gravity wave E_p are apparent, however. Sato et al. (2012, their Figure 2) showed maximum E_p directly over the mountains of the southern Andes at 10 hPa. Likewise, Yan et al. (2010, their Figure 5) revealed similar distributions of mean gravity wave amplitude T' from HIRDLS data that also maximised over the mountains and slowly decreased eastward. In our results, we see some enhancement over the mountains in the height range 26-36 km ($\sim$22-5 hPa) in Figure 2, but maximum values are usually observed well to the east over the oceans during 2010. Other years show similar distributions (omitted for brevity).

One possible explanation may relate to the range of vertical wavelengths to which our analysis method is sensitive. For mountains waves, vertical wavelengths directly over the mountains can be quite long (e.g. Alexander and Teitelbaum, 2011). As previously discussed, our analysis method is primarily sensitive to waves with $4 \gtrsim \lambda_Z \gtrsim 13$ km, and significant amplitude underestimation occurs for waves with $\lambda_Z \gtrsim 13$ km. It could be that the contribution of these long λ_Z waves directly over the mountains to the E_p distributions in Figure 2 is underestimated by our analysis method.

Sato et al. (2012) also observed regions of downward energy flux. In particular they found that, in the region immediately eastward of the southern tip of South America, up to 10% of the E_p distribution consisted of downward propagating waves. This suggests that some of the E_p in our observed distribution may correspond to waves that are propagating downward.

The sources of waves in the long leeward region of increased E_p are currently a topic for debate. As mentioned above, Sato et al. (2012) suggested that increased E_p over 70°W-180°E could be primarily due to mountain waves from the southern Andes and Antarctic Peninsula that have been advected downwind, but the rest of the enhancement was likely the result of other mechanisms. Other studies suggest that much of the enhancement is primarily the result of non-orographic wave sources in and around the Southern

Ocean (e.g. Hendricks et al., 2014; Preusse et al., 2014). Furthermore, the distribution of increased E_p in Figure 2 is very reminiscent of southern hemisphere storm tracks (Hoskins and Hodges, 2005). It is thus likely that the observed distribution of E_p is the result of a number of orographic and non-orographic processes, each playing different roles in different geographical regions. In the next section we use an extended altitude range to build vertical cross-sections of stratospheric E_p in the long leeward distribution to investigate this further.

2.2 Vertical distribution of E_p over the southern Andes and Antarctic Peninsula

An interesting result discussed by Sato et al. (2009) and presented in Sato et al. (2012) was the apparent focusing of gravity waves into the southern stratospheric jet in the Kanto GCM. In a meridional cross-section from 30°S-70°S centred on 55°W (their figure 13), Sato et al. showed increased E_p values in a distinct slanted vertical column over the southern Andes during 5 days in August. Energy flux vectors showed a large flow of energy ∼1500-2000 km southward over the height region 100 hPa (∼16 km) to 1 hPa (∼48 km). The flow appeared to focus towards the centre of the jet, where mean zonal winds were strongest.

In our Figure 3, we select a thin meridional cross-section of normalised monthly-mean COSMIC E_p for August 2010 centred on 65°W. This is close to the cross-section used by Sato et al. (2012). Since raw E_p is expected to increase with increasing altitude and decreasing pressure, each height level in Figure 3 has been normalised such that the lowest value is equal to 0 and the highest value is equal to 1 (Wright and Gille, 2011). This approach highlights the vertical structure. Although temperature profiles from COSMIC typically exhibit increased noise above around 40 km, the normalisation and the increased number of measurements in the month-long time window potentially allow us to resolve large persistent features at higher altitudes, albeit with caution.

A slanted vertical column of increased E_p in the height region 22-35 km and a near vertical column from 35-50 km is evident in Figure 3. The lower section of the column traverses nearly 1500 km southward over the height region 22-35 km. This suggests a clear focusing effect similar to the one suggested by Sato et al., although we cannot recover energy flux information from COSMIC. A monthly-mean zonal wind field $\bar{U}$ (thick contours) from ECMWF operational analysis is used in Figure 3 to show the approximate position of the southern stratospheric jet over the southern Andes and Antarctic Peninsula during August 2010. The gradient of the southward slant in E_p is greatest when the horizontal gradient in zonal wind speed is greatest, such that waves appear to be focused into the centre of the stratospheric jet. This observation is consistent with meridional ray-tracing analyses in the Kanto model (Watanabe et al., 2008; Sato et al., 2009, 2012). Above ~35 km the horizontal gradient in zonal mean wind speed is low and waves appear to generally propagate upward without further latitudinal drift.

This result suggests that waves observed at around 30-40 km over the southern tip of South America and the Drake Passage may have sources further north. In a ray-tracing analysis for an idealized background zonal wind field, Sato et al. (2012, their Figure 5) showed that zero ground-based phase velocity waves with $\lambda_H = 300$ km launched from the southern Andes could propagate eastward and southward by up to around 2500 km and 1000 km respectively before reaching an altitude of 40 km. They found that waves launched from north of 45°S did not propagate upward due the mean wind being too weak. Our results suggest that such waves may indeed propagate from sources north of 45°S, since the slanted column in Figure 3 is observed all the way down to 22 km over 30-45°S . This could imply that there are significant time periods where the tropospheric zonal winds are strong enough to allow vertical propagation of mountain waves from these sources.

An important consideration of this work is the effect of the range of gravity wave vertical wavelengths to which our observations and analysis are limited. For mountain waves

$$\lambda_Z \approx \frac{2\pi U_{||}}{N} \tag{4}$$

where $U_{||}$ is the component of mean wind speed $\bar{U}$ parallel to the wave's horizontal wavenumber vector and N is the local Brunt-Väisälä frequency (Eckermann and Preusse, 1999, Eq.1). Our analysis is primarily sensitive to waves with $4 \gtrsim \lambda_Z \gtrsim 13$. From Equation 4, mountain waves could have vertical wavelengths too long to be detected for $U_{||} \gtrsim 40 -$

50 ms^{-1}. However, horizontal wavenumber vectors of mountain waves over the southern tip of South America have been shown to rotate southwards poleward of 45°S over the Drake Passage (e.g. Alexander and Teitelbaum, 2011). Here, the mean wind vector $\bar{U}$ and the horizontal wavenumber vector are no longer parallel and shorter vertical wavelengths are not precluded since $U_{||}$ is reduced. Therefore the slanted vertical column of E_p in Figure 3 could be due to mountain waves and could suggest meridional propagation.

Sato et al. also suggested that a symmetric northward focusing effect may occur for orographic waves from the Antarctic Peninsula. We investigated such an effect using COSMIC data. Though a slight suggestion of northward meridional focussing may be evident (not shown), we could not find an effect so clear as is observed over the southern Andes.

2.3 Vertical distribution of E_p over the Southern Ocean

We also investigate the vertical distribution of wave energies over the Southern Ocean. Figure 4 shows altitude-normalised E_p in a zonal cross-section from $40-60$°S during August 2010. As in Figure 3, E_p is normalised at each height level in order to highlight the vertical structure.

The vertical column of increased E_p located around 70°W in Figure 4 is the projection in the zonal domain of the vertical column evident in Figure 3. This column is highly suggestive of intense localised mountain wave activity from the southern Andes. The relative intensity of this column at lower altitudes suggests that, within the observational filter of our COSMIC analysis, the southern Andes is the dominant source of orographic wave activity in this latitude band. If small mountainous islands in the Southern Ocean are also significant orographic sources, as has been suggested in recent studies (Alexander et al., 2009; McLandress et al., 2012; Alexander and Grimsdell, 2013), then it is likely that waves from these islands either (1) fall outside the observation filter of our analysis; (2) have small amplitudes; or (3) are too intermittent over monthly time-scales to be revealed in our analysis.

The column at 70°W appears to persist over the full height range in Figure 4. However, between 25-35 km the largest values are observed well eastward, between 60°E-60°W. These peaks are located in a deep region of increased E_p between 20-40 km and 30°W-

90°E, which is the projection in the vertical domain of the long leeward region of increased E_p seen in Figure 2.

At first glance, Figure 4 suggests that this long leeward region of increased E_p is strongly associated with mountain waves from the southern Andes and Antarctic Peninsula region. The lack of significant gravity wave energies upwind (westward) of the mountains and the intensity of energies downwind (eastward) is clear. Sato et al. (2012) suggested that the leeward distribution of increased E_p might be the result of primary mountain waves from the southern Andes and Antarctic Peninsula that have been advected downwind. However, Sato et al. also showed that waves with λ_H<350 km rarely travelled further east than the prime meridian via this mechanism, even under ideal conditions. This suggests that if downwind-advected orographic waves do contribute to the region of increased E_p eastwards of the prime meridian, they likely have $\lambda_H \gtrsim$350 km. Primary orographic waves from the southern Andes and Antarctic Peninsula may also contribute through secondary mechanisms, such as the local generation of waves around the stratospheric jet through breaking or other wave-mean flow interactions (Bacmeister and Schoeberl, 1989). Waves generated by in-situ instabilities and spontaneous adjustment around the stratospheric may also play a part.

Hoskins and Hodges (2005) presented a detailed view of southern hemisphere storm tracks in ECMWF Re-Analysis (ERA-40) data. During austral winter, storms generally tended to maximise over the southern Atlantic and Indian sectors, spiralling poleward and eastward over the Pacific sector. Such storm-tracks may indicate intense sources of non-orographic wave activity. O'Sullivan and Dunkerton (1995) showed that non-orographic waves generated around the tropospheric jet can have vertical wavelengths of a few kilometres. These wavelengths may be too short to be resolved by COSMIC. Mean zonal wind generally increases with height as seen in Figure 4. This may refract these waves to longer vertical wavelengths such that they become visible to COSMIC. This could explain the relative reduction of wave activity at low altitudes over 30°W to 120°E in Figure 4. The spiralling effect of the storm-tracks might also mean that these intense sources of non-orographic waves may begin to move poleward out of the latitude band used in Figure 4. This may explain the relative decrease in intensity further eastward.

We suspect therefore that the leeward region of increased E_p over 70°W-90°E in Figure 4 is likely dominated by (1) primary orographic waves with $\lambda_H > 350$ km from the southern Andes or Antarctic Peninsula that have been advected downwind; (2) secondary waves with non-zero phase speeds generated in the breaking zones of primary orographic waves; and (3) non-orographic wave activity associated with storm tracks over the oceanic sectors. Note that due to vertical resolution limitations, these results may underestimate the contribution of (3). They also do not preclude the existence of other non-orographic sources in the region such as jet instabilities or spontaneous adjustment mechanisms.

3 Individual waves

The long leeward region of increased E_p observed over the southern Atlantic and Indian Oceans is a persistent feature each year during austral winter, though some interannual variability exists. Multiple year averages are one way to learn about dominant processes in a region, but in order to investigate properties of a specific wave field, such as vertical wavelength or wave amplitude, a key question must first be answered: is a wave present? Once this has been answered, it becomes possible to investigate the distribution and species of individual gravity waves in a geographical region.

3.1 Wave identification (Wave-ID) methodology

This section describes our methodology for identifying individual gravity waves from COSMIC GPS-RO temperature profiles. The method is illustrated for an example profile in Figure 5.

We begin by extracting temperature perturbations $T'(z)$ from each profile (Figure 5a) as described in Section 2. We then window the profile with a Gaussian of Full Width at Half Maximum (FWHM) 22 km centred at a height of 30 km (Figure 5b). The purpose of this step is to focus on the height range of the profile most appropriate for gravity wave study using COSMIC GPS-RO data. This height range is chosen to generally correspond to the largest vertical region where (1) the error in bending angle is low; (2) we are unlikely to encounter spurious temperature perturbation anomalies due to incomplete background removal around the tropopause; and (3) retrieval errors associated with ionospheric effects are low (see Tsuda et al., 2011). This corresponds to a region typically between 20-40 km. The choice of a Gaussian window minimises edge effects that may arise in subsequent spectral analysis.

We normalise the windowed profile such that the root-sum-square (RSS) " energy" of the profile is equal to 1 (Figure 5c). Note that the term "energy" is defined as the sum-square of the values of the windowed profile and does not take any other physical meaning here. We then set the average of the profile to zero, and compute the Continuous Wavelet Transform (CWT) of the windowed, normalised and zero-averaged profile. For scale parameter a and position along the profile b, the spectral coefficients $C(a,b)$ of the CWT are given as

$$C(a,b) = \frac{1}{\sqrt{a}} \int_{-\infty}^{\infty} T'(z)\psi^* \left(\frac{z-b}{a}\right) dz \tag{5}$$

where $T'(z)$ is our normalised, windowed and zero-averaged perturbation profile and ψ^* is the complex conjugate of the analysing wavelet. We choose an 8$^{\text{th}}$ order complex Gaussian wavelet for ψ, such that phase information is retained. For such a Gaussian wavelet, scale parameter a, which corresponds to a "stretching" of the wavelet, is approximately related to wavelength λ by

$$\lambda \approx \frac{a\Delta z}{f_{cent}} \tag{6}$$

where Δz is sampling interval and f_{cent} is the dominant central frequency of the wavelet for scale parameter $a = 1$ and unit integer interval spacing ($\Delta z = 1$). Position along the profile b corresponds to altitude z at intervals of Δz.

We are thus able to describe the spectral coefficients $C(a,b)$ in terms of vertical wavelength λ_Z and altitude z. The absolute magnitudes of the spectral coefficients $|C(\lambda_Z,z)|$ are plotted in Figure 5d.

As a result of the normalisation and zero-averaging, the absolute magnitudes of these coefficients can be interpreted as coefficients of pseudo-correlation, describing the correlation between the profile and a wavelet of wavelength λ_Z at altitude z. Ranging between 0 and 1, high (low) values of $|C(\lambda_Z, z)|$ imply the presence (absence) of a clear wave-like feature in the profile.

If the profile and the analysing wavelet are both real, both have RSS " energy" equal to 1 and are both zero-averaged, then the coefficients of the CWT can be exactly interpreted as coefficients of correlation is the usual sense. The coefficients in our analysis are strictly pseudo-coefficients of correlation, due to our choice of a complex wavelet. This choice has the advantage of producing one single peak per wave-like feature in Figure 5d, which is easier to interpret than a series of peaks corresponding to correlation/anti-correlation which would result from a non-complex wavelet.

To positively identify a wave in the profile, we require that the absolute magnitude of the spectral peak coefficient $C_{\text{max}} = \max(|C(\lambda_Z, z)|)$ is greater than or equal to 0.6. This choice is somewhat arbitrary, but it can be interpreted as a requirement that the profile is pseudo-correlated with a wavelet of wavelength λ_Z at position z with coefficient greater than 0.6. If this condition is satisfied, the identification is positive and we record the vertical wavelength λ_{peak} and altitude z_{peak} at C_{max}. As a result of the Gaussian windowing, z_{peak} is almost always located within one wavelength λ_{peak} of 30 km altitude, hence it is reasonable to consider this analysis method as sensitive to gravity waves at a height of around 30 km.

C_{max} can thus be regarded as a confidence metric for the existence of wave-like features in COSMIC perturbation profile. In the example in Figure 5d, the absolute spectral peak $C_{\text{max}} \approx 0.64$ such that a wave with $\lambda_Z \approx 7.1$ km is positively identified at an altitude near 30 km. Information regarding the wave's amplitude T' cannot strictly be obtained from the CWT, so in order to obtain an estimate of T' we find the maximum amplitude of the temperature perturbation profile $T'(z)$ over the height region $z_{\text{peak}} \pm \lambda_{\text{peak}}/2$. In the example in Figure 5b, $T' \approx 2.3$ K.

To summarise our requirements for a positive wave identification, we require that the wave (1) has an amplitude 1 K < T' < 10 K; (2) has a vertical wavelength 2 km < λ_{peak} <

20 km; (3) is located such that 20 km < z_{peak} < 40 km; and (4) has a confidence metric $C_{\text{max}} \geqslant 0.6$ as described above.

Using these criteria, we find that on global year-long average around 20-40% of profiles contain an indentifiable gravity wave signal. In some regions and seasons, as will be seen later, this fraction can be as high as $\sim 80\%$. This wave identification method will be henceforth described as the Wave-ID method for convenience. Note that we currently limit this Wave-ID methodology to one (the dominant) wave per profile.

We note that this method preferentially selects profiles that contain a single large amplitude monochromatic wave with low levels of disassociated noise. A superposition of two waves of equal amplitude may result in neither being identified due to the confidence metric described above. This may also affect our amplitude estimation. However on average it is equally likely that the amplitude will increase or decrease as a result of any superposition. Hence if a sufficient number of profiles are measured, this effect should average out. Wright and Gille (2013) showed that in the southern hemisphere during austral winter, and particularly in the vicinity of the southern Andes and Antarctic Peninsula, there were typically fewer overlapping waves than any other geographical region. Hence, wave identification problems associated with wave superposition are likely minimised in our geographical region of interest.

The choices we have made in our Wave-ID processing will also affect the range of vertical wavelengths we detect. Figure 6 shows transmission curves as a function of wavelength for each processing step in the Wave-ID method. As shown by the net transmission curve (black solid) in Figure 6, the combined analysis method is generally sensitive to gravity waves with 4 km < λ_z < 13 km, with a sharp cut-off below 4 km and a more gradual cut-off above 13 km.

The histogram in figure 6 shows vertical wavelengths of gravity waves identified by this method in the region 35-75°S and 0-90°W during June-August 2006-2012. The distribution of observed vertical wavelengths generally follows the net transmission curve of synthetic waves, with peak observations at 7 km < λ < 9 km.

A primary limitation of the Wave-ID method is the limited vertical window, which limits maximum resolvable vertical wavelength. This is due to the limited vertical extent of the high-accuracy temperature retrieval of COSMIC GPS-RO. Extending the region upwards would reduce confidence in any resolved waves due to increased noise in measurements above z $\approx$ 38 km (Tsuda et al., 2011). If we extend the region down much further, sharp gradients in temperature around the tropopause risk introducing spurious artifacts via traditional filtering methods (Alexander and de la Torre, 2011). Furthermore, decreasing wave amplitudes with increasing pressure in addition to the presence of water vapour makes gravity wave study below the tropopause difficult via GPS-RO. We also implicitly assume that λ_Z does not change much with altitude, which might not hold true for the real atmosphere. This could decrease the probability that we will identify waves with longer λ_Z, which may help to explain the slight mis-match between the histogram in Figure 6 and the range of permitted wavelengths (solid black curve) for longer λ_Z waves.

Future work may involve (1) optimising this vertical window so as to resolve the maximum possible range of vertical wavelengths; (2) investigating the optimum threshold value above which to consider a wave identification as positive; and (3) employing methods to identify overlapping waves as described by Wright and Gille (2013).

3.2 Wave identification results

In Figure 7a we present a multi-year composite plot of E_p for June-August 2006-2012 at 30 km over the southern hemisphere. In this analysis, we take the mean E_p from all available profiles, including those where no significant waves are present. In Figure 7b we produce another composite plot of E_p but calculated using only waves identified via the Wave-ID method described above. In other words, Figure 7a is a time-averaged climatology of E_p in the region whereas Figure 7b is the mean E_p of individual waves detected using the Wave-ID method during this period.

An initial observation is that much higher E_p values are apparent in Figure 7b than in Figure 7a. This is expected, since mean E_p values in Figure 7b are skewed by the exclusion of profiles for which no wave-like feature was detected.

The same long leeward region of increased E_p sweeping around Antarctica is present in both panels of Figure 7. The largest values in both panels are generally observed just east of the southern tip of South America and the Antarctic Peninsula, decreasing eastward and reaching a minimum just west of the Drake Passage. By comparison of the two maps from the two different methods in Figure 7, information about wave intermittency can be inferred. The peak of the distribution of E_p in Figure 7b resides much closer to the mountains of the southern Andes and Antarctic Peninsula, but the rest of the distribution remains broadly co-located with the results in Figure 7a. The westward shift of the peak implies that waves close to the southern Andes and Antarctic Peninsula have on average larger amplitudes, but are more intermittent since this peak is diminished in the average of all available profiles. The rest of the distribution may therefore be less intermittent, since it remains broadly co-located in both panels. This is consistent with the hypothesis that the region immediately east of the mountains is dominated by waves from orographic sources, which have been shown to be generally more intermittent than non-orographic sources in this region (Hertzog et al., 2008, 2012; Plougonven et al., 2013; Wright et al., 2013). A small enhancement is also evident at around 160°E 65°S that may be suggestive of a contribution from orographic waves from the Transantarctic Mountains.

To further investigate the nature of the wave field in this long leeward region of increased E_p, we divide the latitude band 40-65°S into six longitudinal sectors A-F, and examine the population of waves in each sector. Sector C contains the mountains of southern Andes, Antarctic Peninsula and South Georgia. Sector B is oceanic and upwind (westward) of these mountains. Sector D is also oceanic but immediately downwind (eastward) of the mountains. Sectors A, E and F are predominantly oceanic. Figure 9 presents histograms of individual wave amplitudes identified using the Wave-ID method in each of these six sectors during June-August 2006-2012. Note that these waves are from the same profiles used to produce the E_p distribution in Figure 7b.

At first glance, the histograms of wave amplitudes in each sector in Figure 9 appear broadly similar. Approximately 20000 waves are identified in each sector and the modal amplitude is between 2-3 K. Upon closer inspection however, some important differences become apparent.

Despite containing around 4.5% and 12% fewer profiles than Sector B respectively, Sectors C and D contain around 13% and 6% more identified waves respectively. This indicates that the sectors containing and immediately downwind of the southern Andes and Antarctic Peninsula (C,D) contain significantly more identifiable waves than sectors immediately upwind. Furthermore, Sector B has the highest number of available profiles, yet the lowest number of identified waves of any sector.

We next investigate the relative distribution of wave amplitudes in each sector compared to the zonal mean to highlight any longitudinal variation in wave amplitude populations. The rightmost panel in Figure 9 shows the difference between the histogram in each sector and the zonal mean histogram of wave amplitudes. The curves in this panel indicate that the sectors containing and downwind of the southern Andes and Antarctic Peninsula (C,D) contain significantly more large amplitude ($3 < T' < 8$ K) waves and fewer small amplitude waves ($T' < 2.5$ K) than the zonal mean, whereas upwind Sectors A, B and F contain fewer large amplitude waves and more small amplitude waves.

Three interesting conclusions are indicated by this analysis. Firstly, the geographical region downwind (eastward) of the mountains of the southern Andes and Antarctic Peninsula up to around 40°E contains significantly more identifiable gravity waves than a region of equal size upwind (westward) of the mountains.

Secondly, this downwind region contains significantly more large amplitude waves with $3 < T' < 8$ K than the corresponding upwind region, though these large amplitude waves are still relatively rare. Since $E_p \propto (T')^2$, it is likely that the structured distribution of E_p in Figure 7b is hence the result of an increased number of large amplitude mountain waves immediately downwind of the southern Andes and Antarctic Peninsula. In a recent study involving balloon, satellite and mesoscale numerical simulations above Antarctica and the Southern Ocean, Hertzog et al. (2012) showed that rare, large amplitude waves are not only more commonly observed above mountains in this region but that these events represent the main contribution to the total stratospheric momentum flux during the winter regime of the stratospheric circulation. Hertzog et al. also showed that gravity waves populations over open ocean tend to follow a more log-normal distribution with fewer rare, large amplitude events. Our results reinforce the findings of Hertzog et al..

Thirdly, and perhaps most interestingly, differences in the number of identified waves and the relative distribution of wave amplitudes between sectors are significant, but relatively small in absolute terms. In general, each sector has strikingly similar distributions of wave amplitudes and total numbers of identified waves. This zonal uniformity in the distributions of wave amplitudes may be suggestive of strong, zonally uniform source mechanisms for gravity waves in all sectors, such as spontaneous adjustment or jet instability around the edge of the southern stratospheric jet. This is discussed further in Section 5.

4 Gravity wave momentum fluxes during JJA 2006 using COSMIC profile pairs

Gravity wave momentum flux is one of the key parameters characterising the effects of gravity waves in the atmosphere. This is of vital importance to the gravity wave modelling community, but typically difficult to obtain from observations (Fritts and Alexander, 2003; Alexander et al., 2010). Ern et al. (2004) showed that an approximation to the absolute value of momentum flux can be inferred from satellite observations of a gravity wave's amplitude T' and horizontal and vertical wavenumbers k_H and m. In the case of limb-sounding instruments such as HIRDLS and CRISTA, T' and m can be obtained directly from a single vertical temperature profile, while k_H can be estimated using the phase shift between adjacent profiles (Ern et al., 2004; Alexander et al., 2008). However, such k_H estimation methods have not routinely been applied to COSMIC, due to typically large inter-profile spacing. The scarcity of multiple profiles that are both closely spaced and closely timed with near-parallel lines of sight limits the accurate estimation of k_H in this way. Wang and Alexander (2010) investigated the use of 3 or more COSMIC profiles to make estimates of zonal and meridional horizontal wavenumbers k and l. However, as discussed by Faber et al. (2013), limitations in sampling density, aliasing and differing lines of sight restrict their approach being used in the general case.

Here we investigate an alternative approach for estimation of k_H from COSMIC GPS-RO data using a modified form of the method described by Alexander et al. (2008). We take advantage of the deployment phase of the COSMIC constellation, when pairs of satellites were often physically close (Liou et al., 2007). During this phase, a single occulting GPS satellite was often tracked by a close pair of COSMIC satellites, resulting in a significant number pairs of profiles that were closely spaced and closely timed, with near-parallel lines of sight. These particular profile pairs permit the use of a k_H estimation method and subsequently an estimation of gravity wave momentum flux. k_H has also been determined in a similar manner in recent studies by McDonald (2012) and Faber et al. (2013). In this section, we use this method to make estimates of gravity wave momentum flux from COSMIC GPS-RO during June-August 2006 over the southern Andes, Drake Passage and Antarctic Peninsula.

4.1 Profile pair selection and processing

First, we identify profile pairs during June-August 2006 that are closely spaced, closely timed and have near-parallel lines of sight. We require that the two profiles must (1) be horizontally separated by less than 300 km at a height of 30 km; (2) be separated in time by less than 15 minutes; and (3) have lines of sight aligned within 30° of each other. The line of sight requirement is important since we require that waves have $\lambda_H \geqslant 270$ km in the line of sight as discussed in Section 1.1.1. If the two viewing angles differ by a large amount, the same wave might not be observable in both profiles. Finally, we require that a clear wave-like feature of approximately the same vertical wavelength (± 1.5 km) is identified in both profiles using the Wave-ID method described in section 3.1. A discussion of this vertical wavelength criterion as an identification method for the same wave in both profiles is provided by McDonald (2012).

In practise, we find that the majority of profile pairs during June-August 2006 have horizontal separations ~10 km (see Figure 12a), time separations of less than a minute and lines-of-sight separated by less than 1°. Hence requirements (1), (2) and (3) are usually satisfied. The requirement that both profiles contain the same wave-like feature reduces the number of available pairs from $\sim$75000 to $\sim$14000 globally during June-August 2006. Of these, around 1300 lie in our geographical region of interest.

To estimate k_H in each profile pair, we follow a modified form of the method described by Alexander et al. (2008). We first apply a Gaussian window of FWHM = 22 km centred at 30 km altitude as described in section 3.1. We next compute the CWT of each profile. The resulting transform $\tilde{T}(z, \lambda_Z)$ is a complex valued function of altitude z and vertical wavelength λ_Z. For the two profiles a and b, the cospectrum $C_{a,b}$ is computed as

$$C_{a,b} = \tilde{T}_a \tilde{T}_b^* = \hat{T}_a \hat{T}_b e^{i\Delta\phi_{a,b}} \tag{7}$$

where $\hat{T}$ is the magnitude and $\Delta\phi_{a,b}$ is the phase difference between the two profiles for each λ_Z at each position z. The covariance spectrum is the absolute value $|C_{a,b}|$. We locate the maximum in the covariance spectrum C_{max} in the height region 20-40 km, for vertical wavelengths less than 18 km. The location of C_{max} in the covariance spectrum corresponds to the dominant vertical wavelength λ_{DOM} common to both profiles at altitude z_{DOM}. We then compute the phase difference between the two profiles $\Delta\phi_{a,b}$ as

$$\Delta\phi_{a,b} = \arctan\left(\frac{\text{Im}(C_{a,b})}{\text{Re}(C_{a,b})}\right) \tag{8}$$

where $\text{Re}(C_{a,b})$ and $\text{Im}(C_{a,b})$ are the real and imaginary coefficients of the covariance spectrum $C_{a,b}$. We record the value of $\Delta\phi_{a,b}$ at C_{max}.

We then compute the projection of the horizontal wavenumber k_H along the horizontal axis joining the two profiles a and b as

$$k_H = \frac{\Delta\phi_{a,b}}{\Delta r_{a,b}} \tag{9}$$

where $\Delta r_{a,b}$ is the horizontal separation of profiles a and b at around 30 km altitude. We then compute $\lambda_H = 2\pi/k_H$. This projected value of λ_H is typically longer than the true horizontal wavelength, and hence represents an upper-bound estimate (Ern et al., 2004). A useful illustration of this geometry can be found in (Preusse et al., 2009). We require that $100 \leqslant \lambda_H \leqslant 5000$ km to exclude unphysically short or extremely long horizontal wavelengths. This exclusion is discussed in more detail in Appendix A.

Generally, the horizontal separation Δr of our profile-pairs is much shorter than the LOS horizontal resolution $\Delta L \sim 270$ km. Therefore, any phase difference measured between the profiles is not likely to be the result of phase difference in the LOS direction, but the result of phase difference perpendicular to the LOS. For this reason we take Δr to be the perpendicular horizontal separation of the pair with respect to the LOS or the first profile in each pair. This is generally close to the absolute horizontal separation due to the geometry of the constellation during the deployment phase.

To obtain an estimate of wave amplitude T', we find the maximum amplitude in each perturbation profile $T'_a(z)$ and $T'_b(z)$ over the height region $z_{\mathrm{DOM}} \pm \lambda_{\mathrm{DOM}}/2$, and take the mean.

Finally we compute an estimate of the absolute value of momentum flux M_{flux} as

$$M_{\mathrm{flux}} = \frac{\bar{\rho}}{2} \frac{\lambda_Z}{\lambda_H} \left(\frac{g}{N}\right)^2 \left(\frac{T'}{\bar{T}}\right)^2 \tag{10}$$

where $\bar{\rho}$ is local atmospheric density, g is acceleration due to gravity and N is the Brunt-Väisälä (buoyancy) frequency.

4.2 COSMIC momentum flux results

Figure 10 shows gravity wave vertical wavelengths, horizontal wavelengths and momentum flux from our COSMIC pair analysis over the southern Andes, Drake Passage and Antarctic Peninsula during June-August 2006. Also shown are coincident results from HIRDLS, using the Stockwell Transform (S-Transform Stockwell et al., 1996) method described by Alexander et al. (2008) modified by Wright and Gille (2013). COSMIC and

HIRDLS are sensitive to broadly overlapping parts of the gravity-wave spectrum, so we provide results from HIRDLS as a comparison.

In Figure 10a, our COSMIC analysis shows longer mean vertical wavelengths over the southern tip of South America extending south over the Drake Passage. This southward extension out over the Drake Passage is in good agreement with a case study of a large mountain wave event in the region by Alexander and Teitelbaum (2011), using data from the Atmospheric InfraRed Sounder (AIRS) instrument. They did however infer longer vertical wavelengths due to the deep vertical weighting function of the AIRS instrument and the assumption of zero ground-based phase velocities. This region of longer vertical wavelength also extends further south over the Antarctic Peninsula.

The corresponding HIRDLS analysis in Figure 10d shows typically longer λ_Z values overall, likely due to the increased sensitivity of HIRDLS to waves with long λ_Z as a result of the larger usable height range in HIRDLS profiles. Like our COSMIC analysis, Figure 10d also shows longer mean vertical wavelengths over the southern tip of South America. However, a region of longer vertical wavelengths is also evident between 80-100°W that is not seen in our COSMIC analysis. We do not fully understand the reasons for this, but we suspect that it may be due to differing vertical wavelength sensitivities of HIRDLS and COSMIC. A full investigation into the distributions of vertical wavelengths from the HIRDLS S-Transform analysis is however beyond the scope of this study.

The results of our λ_H analysis from COSMIC profile-pairs is presented in Figure 10b. We mostly observe values of around 600-800 km, but no structured geographical pattern is evident. We suspect this distribution (or lack thereof) may be due to the viewing geometry of GPS-RO technique, more specifically the orientation of the horizontal axis joining the two profiles in each profile pair, which can vary significantly between pairs. Since the measured horizontal wavelength is the projection of the true λ_H along the axis between the two profiles, it is a upper-bound estimate heavily dependent the orientation of this horizontal axis. Even in a region where the wave field has a preferential horizontal alignment we will still recover a range of horizontal wavelength estimates due to differing orientations. HIRDLS scan-tracks are more consistently aligned ~NW-SE or ~NE-SW across this region, and hence estimates of λ_H between adjacent HIRDLS profiles will be more consistent, but not necessarily more accurate. This is likely the reason that the more structured geographical distribution of λ_H shown in HIRDLS results, where shorter horizontal wavelengths are observed generally south and east of the southern tip of South America, is not observed by COSMIC.

The absolute values of our λ_H analysis are however physically reasonable and in good agreement with other studies such as Ern et al. (2004). They are however much shorter than HIRDLS estimates. Our COSMIC profile-pairs typically have smaller horizontal separations ($\sim$10 km) between profile-pairs than HIRDLS ($\sim$80 km for an ascending-descending pair, $\sim$120 km for a descending-ascending pair (e.g. Wright et al., 2015)). This means that any absolute error in phase difference $\Delta\phi_{a,b}$ between COSMIC pairs will bias our results towards shorter λ_H than might be found in a HIRDLS profile-pair. We suspect that this may be the reason we observe lower absolute horizontal wavelength values in our COSMIC analysis than in HIRDLS. The results are not contradictory however, since both estimates represent an upper-bound. This sensitivity to errors in phase difference and their effect on λ_H estimation with regards to horizontal separation is discussed more fully in Appendix A.

Figure 10c shows the results of our COSMIC momentum flux analysis. Two local maxima of order 10^{-2} Pa are observed over the southern tip of South America and the Antarctic Peninsula. This increased flux over the southern tip of South America is in good agreement with results from CRISTA (Ern et al., 2004) and HIRDLS (Alexander et al., 2008) and the maximum over the Antarctic Peninsula is in good agreement with results from the Vorcore superpressure balloon campaign presented in Hertzog et al. (2008). Hertzog et al. showed that most of the momentum flux in the maximum over the Antarctic Peninsula was in a westward direction, suggestive of orographic gravity waves propagating against the mean stratospheric flow. Increased momentum flux is also observed to the east of the two maxima, suggestive of significant wakes of associated gravity wave flux downwind from these sources.

The HIRDLS analysis Figure 10f shows a maximum over the southern tip of South America, consistent in location and magnitude with our COSMIC results. HIRDLS estimates of gravity wave momentum flux are slightly higher, though this could be somewhat expected since the HIRDLS analysis method used here generally resolved waves with longer vertical wavelengths than the COSMIC method. The COSMIC analysis is able to identify a secondary maximum over the Antarctic Peninsula which is not observed by HIRDLS due to the lack of measurements poleward of 62°S.

These momentum flux measurements reaffirm that the southern Andes and Antarctic Peninsula are intense and persistent sources of gravity wave momentum flux during austral winter. Perhaps more importantly however, our results demonstrate that, given sufficient sampling density, COSMIC GPS-RO can provide physically reasonable estimates of stratospheric gravity-wave momentum flux that are consistent with results from HIRDLS, CRISTA and Vorcore. The final configuration of the COSMIC constellation however restricts the number of suitable profile-pairs such that regional climatological studies of gravity wave momentum flux using our method are generally limited to the deployment phase in 2006. However, as discussed in Section 5, dramatically increased sampling density provided by upcoming radio occultation missions may provide an opportunity to apply this method on a global scale in coming years.

5 Discussion

During austral winter in the southern hemisphere, the mountains of the southern Andes and Antarctic Peninsula are a known hot spot of gravity wave fluxes (e.g. Alexander and Teitelbaum, 2007, 2011; Hoffmann et al., 2013). However, the origin of the long leeward distribution of enhanced gravity wave energy stretching eastwards far over the ocean is currently a topic for debate.

As discussed in Section 2.3, Sato et al. (2012) suggested that waves from the mountains of the southern tip of South America and northern tip of the Antarctic Peninsula can propagate significantly downwind if their horizontal wavenumber vectors are aligned at an acute angle to the mean stratospheric flow. However, using a ray-tracing analysis Sato et al. also showed that for horizontal wavelengths of 250-350 km such waves rarely propagate east of the prime meridian, regardless of launch angle. Hence, the distribution of increased E_p shown here eastwards of around 20°E is not likely to be explained by the downwind propagation of waves with λ_H less than approximately 350 km. This suggests that the distribution of increased E_p eastwards of around 20°E may be the result of (1) downwind propagating mountain waves with λ_H > 350 km; (2) locally generated non-orographic waves from tropospheric or stratospheric sources out over the ocean; or (3) some combination of these processes.

Preusse et al. (2014) used backwards ray-tracing of resolved waves in ECMWF data to show that during August 2008, waves over the southern Andes and Antarctic Peninsula overwhelmingly had lowest traceable altitude (LTA) values close to the surface, whereas waves over the southern Atlantic and Indian oceans often had average LTA values around 7-12 km. Their results are indicative of upper-tropospheric non-orographic wave sources that exist out over the oceans. Similarly, Hendricks et al. (2014) suggested that a belt of increased stratospheric gravity wave activity observed by AIRS could be attributed to non-orographic sources in winter storm tracks around the southern Atlantic and Indian Oceans. The distribution of increased stratospheric E_p in our Figure 2 is morphologically reminiscent of southern hemisphere storms tracks in ECMWF ERA-40 data presented by Hoskins and Hodges (2005), which may support the suggestion by Hendricks et al.. Our Figure 4 suggests that if waves from these sources significantly contribute to the region of increased stratospheric E_p over these oceans, then these waves generally have λ_Z too short ($\lesssim$ 3 km) to be resolved by COSMIC below ~20 km altitude. As these waves ascend, the mean wind speed increases and they might be refracted to longer vertical wavelengths such that they may be resolved and can contribute to the E_p in Figures 2 and 4. It should be noted however that the waves considered by Preusse et al. in ECMWF data are typically below the height region considered in this study, and the waves observed by Hendricks et al. in AIRS data are not typically visible to COSMIC.

In Section 2.2 we presented evidence of a southward focussing of gravity waves into the centre of the stratospheric jet. In a recent modelling study, McLandress et al. (2012) showed that zonal wind biases and vortex breakdown timing errors in a latitude band near

60°S could be greatly reduced in the Canadian Middle Atmosphere Model (CMAM) through the inclusion of non-specific orographic gravity wave drag (GWD) in the stratosphere. One hypothesis for the missing drag is unparametrized mountain waves from small islands in and around the Southern Ocean that are sub-gridscale in CMAM. A second hypothesis is the southward (northward) propagation of orographic waves from the north (south) into the southern stratospheric jet from outside the latitude band (McLandress et al., 2012; Preusse et al., 2014). Our results suggest evidence of such meridional propagation. In particular, we observe a southward focusing of waves in Figure 3 into the jet around 60°W from sources further north, supporting the second hypothesis described above. It is conceivable that there exists a similar process whereby waves from the Antarctic Peninsula are focussed northwards into the jet, though we are unable to find such clear evidence for this in our results. Observational evidence of any meridional focusing is significant since many parametrization schemes used operationally in GCMs do not include such focussing phenomena (Preusse et al., 2014).

In Section 3 we investigated longitudinal variations in wave populations in the long leeward region of increased E_p during June-August 2006-2012. In regions immediately downwind of the southern Andes and Antarctic Peninsula we observe significantly more rare, large amplitude waves than in upwind regions, while only a slight increase in the absolute number of waves is observed. Further analysis (omitted for brevity) showed that exclusion of these large amplitude waves resulted in a much more zonally uniform distribution of mean wave energy around over the Southern Ocean. This suggests that the increased E_p observed immediately downwind of the mountains in Figure 7b is the result of increased numbers of rare, large amplitude wave events in this downwind region and not simply the result of more waves in general. As discussed in Section 3.2, this is consistent with the results of a super-pressure balloon and modelling study by Hertzog et al. (2012). The eastward decrease in E_p values in Figure 7b correlates well to the eastward decrease of the frequency of occurrence of these rare, large amplitudes waves.

However, the general distributions of gravity wave amplitudes at all longitudes in the latitude band 40-65°S are broadly similar. This may be indicative of persistent, zonally uniform non-orographic source mechanisms in and around the stratospheric jet. Inertia-gravity waves, to which GPS-RO is preferentially sensitive, can often be generated at the edge of jet streams via spontaneous adjustment processes (Fritts and Alexander, 2003). Hence, a possible contribution to the long leeward region of increased E_p in Figure 7b may be from gravity waves generated via these adjustment mechanisms.

In the context of other studies, our results therefore suggest that the long leeward region of increased E_p consists of (1) rare, large amplitude waves over 80°W-40°E from orographic sources such as the southern Andes and Antarctic Peninsula that may also have been meridionally-focussed and advected downwind; (2) a possible contribution secondary waves generated locally in the breaking region of these primary orographic waves; (3) a possible contribution from non-orographic waves from sources associated with winter storm tracks over the southern oceans; and (4) a zonally uniform distribution of small amplitude waves from non-orographic mechanisms such as spontaneous adjustment and jet instability around the edge of the stratospheric jet.

Finally, we described a method for the estimation of stratospheric gravity wave momentum flux from COSMIC GPS-RO. To our knowledge, there are very few studies that have successfully developed methodologies for gravity wave momentum flux estimates from GPS-RO data (e.g. Wang and Alexander, 2010; Faber et al., 2013). Our results demonstrate that, given sufficient sampling density, COSMIC GPS-RO can produce physically reasonable estimates of stratospheric gravity wave momentum flux over the southern Andes and Antarctic Peninsula that are consistent with results from CRISTA, HIRDLS and Vorcore (Ern et al., 2004; Alexander et al., 2008; Hertzog et al., 2008). It is important to note that our results have a bias towards shorter horizontal wavelength estimation for reasons discussed in Appendix A.

The method presented here is mostly limited to the deployment phase of the COSMIC constellation only, since the number of profile-pairs that satisfy the requirements outlined in Section 4.1 is very low once the satellites reached their final configuration.

However, GPS-RO is an expanding technique, with new missions scheduled for launch in the next decade. The 12-satellite COSMIC-2 constellation (Cook et al., 2013) will boast more than 8000 soundings per day, measuring the occultations of satellites from the European navigation satellite system GALILEO and the Russian Global Navigation Satellite System (GLONASS), in addition to the American GPS satellite constellation. COSMIC-2 will feature two deployment phases from which large numbers of closely spaced profile-pairs can be expected. Furthermore, the number of profile-pairs available from their final configuration is likely to increase significantly and there will be increased coverage in the tropics as a result of 6 low-inclination (24°) satellites.

6 Summary and Conclusions

In this study, we have used dry atmospheric temperature profiles from COSMIC GPS-RO to investigate gravity wave activity in the southern stratospheric hot spot around the southern Andes and Antarctic Peninsula. The new wavelet analysis technique we have presented allows identification of the properties of individual gravity waves, which we have used the determine gravity wave energies, amplitudes, momentum fluxes and variability.

In the hot-spot region, we have found clear evidence of the southward propagation of orographic gravity waves into the strong winds of the southern stratospheric jet. This phenomenon has been predicted by recent high-resolution modelling studies (e.g. Watanabe et al., 2008; Sato et al., 2009, 2012).

We also investigated the long leeward region of increased E_p stretching out over the southern oceans during austral winter. Our results suggest that this region is the result of waves from a number of overlapping orographic and non-orographic sources.

Our results, in the context of other studies, suggest that the long leeward region of increased E_p is the result of waves from a number of overlapping orographic and non-orographic wave sources. We have used the distribution of the amplitudes of individual waves to suggest that the large mean Ep values observed immediately downwind of the southern Andes and Antarctic Peninsula result from an increased number of rare, large amplitude mountain waves that have propagated downwind via the mechanism described by Sato et al. (2012). The remaining distribution is likely to be the result of waves from a variety of non-orographic sources such as storms in and around the Southern Ocean (Hendricks et al., 2014; Preusse et al., 2014) and spontaneous adjustment mechanisms around the edge of the southern stratospheric jet (Fritts and Alexander, 2003; Hei et al., 2008).

We have also described a method for the estimation of k_H from closely spaced pairs of COSMIC profiles measured during the deployment phase of the constellation in July-August 2006. We have also shown that, given sufficient sampling density, estimations of gravity wave momentum flux in the region around the southern Andes and Antarctic Peninsula can be retrieved from COSMIC GPS-RO. These measurements are broadly consistent with results from CRISTA (Ern et al., 2004), HIRDLS (Alexander et al., 2008), and Vorcore (Hertzog et al., 2008). In the coming years, the increased sampling density offered by new GPS-RO missions may allow our approach to be temporally and geographically expanded, potentially providing estimates of stratospheric gravity wave momentum flux on a much wider scale.

Acknowledgements. This study is supported by the UK Natural Environment Research Council (NERC): CJW and NJM are supported by NERC grant NE/K015117/1 and NPH by a PhD studentship awarded to the University of Bath. We are grateful to Andrew Moss for helpful suggestions and discussions. We would also like to acknowledge Harrower and Brewer (2003) for the ColorBrewer colormaps featured in this study.

Appendix A: On the determination of λ_H from COSMIC profile-pairs

The increased number of closely-spaced profile-pairs during the deployment phase of the COSMIC constellation facilitates a focussed momentum flux study in the hot spot region. Many of these profile-pairs have very short horizontal separations $\Delta r \sim 10$ km. The method for the estimation of λ_H described in Section 4.1 is inherently sensitive to error in the determination of vertical phase shift $\Delta\phi$. The short horizontal separation of these pairs may introduce a bias towards shorter horizontal wavelengths. Other than comparing our λ_H estimates to estimates from other studies as in Section 4.2, it is difficult to independently quantify the error and reliability of these estimates. This Appendix discusses the effect of short horizontal separations of COSMIC profile-pairs on the estimation of λ_H in comparison to profile-pairs from the HIRDLS mission.

A1 Horizontal profile-pair separations

An estimate of horizontal wavelength λ_H can be calculated from the horizontal separation and phase difference between two adjacent profile-pairs via the relation in Equation 9. For a given wave field, it would be expected that in general, shorter horizontal separations between profile-pairs would result in smaller phase differences in profile-pairs.

Along the HIRDLS scan-track, vertical profiles are measured in an alternating "upscan" and "downscan" pattern. An illustration of this pattern can be seen in Wright et al. (2015, their Fig. 4b). At an altitude of 30 km, alternating "downscan/upscan (D/U) and "upscan/downscan" (U/D) profile-pairs have horizontal separations of ~80 km and ~120 km respectively (see blue bars in our Figure 12a).

Figure 11 shows histograms of gravity wave phase differences between COSMIC, HIRDLS D/U and HIRDLS U/D profile-pairs during June-August 2006. Planetary wave features were removed from COSMIC profiles via a zonal high-pass filtering method, suppressing zonal wavenumbers $s \leqslant 6$. HIRDLS profile-pairs are processed using the method described by Wright and Gille (2013).

All three horizontal separations in Figure 11 indicate a general preference towards small ($\Delta\phi < \frac{\pi}{8}$) phase differences. To investigate the relative differences between each of the distributions, we normalise each histogram such that the total number of profiles in each is equal to one. We then subtract each normalised distribution from the mean of the three to find the relative difference. The bottom panel of Figure 11 indicates that COSMIC pairs with $\Delta r \sim 10$ km generally have more small ($\Delta\phi < \frac{\pi}{8}$) and fewer large ($\Delta\phi > \frac{\pi}{8}$) phase difference values than HIRDLS pairs. The HIRDLS U/D pairs, with the largest horizontal separation, generally have more large phase differences.

This suggests that, as might be expected, shorter horizontal separations between profile-pairs generally result in smaller phase differences. This result provides a useful sanity-check for the λ_H estimation methodology, particularly its application to COSMIC profile-pairs.

A2 Biases from small phase differences

Even if the methodology is valid for horizontal separations as short as $\sim$10 km, error in the determination of $\Delta\phi$ will have a larger effect, since the method is more reliant on the determination of very small phase differences. If the absolute error in determination of $\Delta\phi$ is $\pm 0.1 \approx \frac{\pi}{30}$ radians, then absolute phase differences of $0 \leqslant \Delta\phi \leqslant \frac{\pi}{30}$ will be indistinguishable from each other. For a COSMIC profile-pair with Δr $\sim$10 km, horizontal wavelengths greater than 600 km projected along the axis joining the profile-pair would therefore be ambiguous due to this error.

The shortest theoretically resolvable horizontal wavelength from a COSMIC profile-pair is twice the horizontal separation, $2 \times \Delta r$ $\approx$20 km. However, the requirement of $\lambda_H \gtrsim$270 km in the LOS direction implies the rare case where the LOS is very closely aligned perpendicular to the horizontal wavenumber vector. Therefore large numbers of these very short λ_H estimates are unlikely to be physical, and an approximate cut-off of $\lambda_H \gtrsim$ 100 km may be more realistic.

For an absolute error in phase difference of $\pm\frac{\pi}{30}$, λ_H estimates from COSMIC profile-pairs with $\Delta r \sim$ 10 km may be accurate for $100 \lesssim \lambda_H \lesssim$ 600 km. For larger horizontal separations and/or more accurate phase difference determinations, the upper limit is larger. Figure 12d shows a density plot of horizontal separation against phase difference for COSMIC profile-pairs in which a wave was identified via the method described in Section 3. Dashed black lines show lines of constant λ_H estimated via the relation in Equation 9. For the majority of detected waves $250 \lesssim \lambda_H \lesssim$ 5000 km. A low-bias effect on the estimation of λ_H for short horizontal separations $\Delta r \sim$ 10 km due to the error in the determination $\Delta\phi$ can be seen in the bottom left corner of the panel.

In summary, we suggest that phase difference estimates from COSMIC profile-pairs from the deployment phase of the constellation are broadly in line with what we might expect when compared to HIRDLS profile-pairs. However, the typically short horizontal separations of the closely spaced COSMIC profile-pairs used in Section 4 are likely to introduce a low-bias in the estimation of λ_H due to error in the determination of $\Delta\phi$. We suspect that this is the reason for the differences in λ_H estimates between COSMIC and HIRDLS in Figure 10e. The estimates are not necessarily contradictory, since both represent an upper bound value, but this bias should be considered when comparing results from the two instruments.

References

Alexander, M. J. and Barnet, C.: Using satellite observations to constrain parameterizations of gravity wave effects for global models., Journal of the Atmospheric Sciences, 64, 1652–1665, doi:10.1175/JAS3897.1, 2007.

Alexander, M. J. and Grimsdell, A. W.: Seasonal cycle of orographic gravity wave occurrence above small islands in the Southern Hemisphere: Implications for effects on the general circulation, Journal of Geophysical Research, 118, 11 589–11 599, doi:10.1002/2013JD020526, 2013.

Alexander, M. J. and Teitelbaum, H.: Observation and analysis of a large amplitude mountain wave event over the Antarctic peninsula, Journal of Geophysical Research, 112, doi:10.1029/2006JD008368, 2007.

Alexander, M. J. and Teitelbaum, H.: Three-dimensional properties of Andes mountain waves observed by satellite: A case study, Journal of Geophysical Research, 116, doi:10.1029/2011JD016151, 2011.

Alexander, M. J., Gille, J., Cavanaugh, C., Coffey, M., Craig, C., Eden, T., Francis, G., Halvorson, C., Hannigan, J., Khosravi, R., Kinnison, D., Lee, H., Massie, S., Nardi, B., Barnett, J., Hepplewhite, C., Lambert, a., and Dean, V.: Global estimates of gravity wave momentum flux from High Resolution Dynamics Limb Sounder observations, Journal of Geophysical Research, 113, D15S18, doi:10.1029/2007JD008807, 2008.

Alexander, M. J., Eckermann, S. D., Broutman, D., and Ma, J.: Momentum flux estimates for South Georgia Island mountain waves in the stratosphere observed via satellite, Geophysical Research Letters, 36, L12 816, doi:10.1029/2009GL038587, 2009.

Alexander, M. J., Geller, M., McLandress, C., Polavarapu, S., Preusse, P., Sassi, F., Sato, K., Eckermann, S., Ern, M., Hertzog, A., Kawatani, Y., Pulido, M., Shaw, T. A., Sigmond, M., Vincent, R., and Watanabe, S.: Recent developments in gravity-wave effects in climate models and the global distribution of gravity-wave momentum flux from observations and models, Quarterly Journal of the Royal Meteorological Society, 136, 1103–1124, doi:10.1002/qj.637, 2010.

Alexander, P. and de la Torre, A.: A method to improve the determination of wave perturbations close to the tropopause by using a digital filter, Atmospheric Measurement Techniques, 4, 1777–1784, doi:10.5194/amt-4-1777-2011, 2011.
Alexander, S. P., Tsuda, T., Kawatani, Y., and Takahashi, M.: Global distribution of atmospheric waves in the equatorial upper troposphere and lower stratosphere: COSMIC observations of wave mean flow interactions, Journal of Geophysical Research, 113, doi:10.1029/2008JD010039, 2008.
Alexander, S. P., Klekociuk, A. R., and Tsuda, T.: Gravity wave and orographic wave activity observed around the Antarctic and Arctic stratospheric vortices by the COSMIC GPS-RO satellite constellation, Journal of Geophysical Research, 114, doi:10.1029/2009JD011851, 2009.
Bacmeister, J. T. and Schoeberl, M. R.: Breakdown of Vertically Propagating Two-Dimensional Gravity Waves Forced by Orography, Journal of the Atmospheric Sciences, 46, 2109–2134, 1989.
Cook, K., Fong, C. J., Yen, N., Wenkel, M. J., Wilezynski, P., and Chang, G. S.: FORMOSAT-7/COSMIC-2 GNSS radio occultation constellation mission for global weather monitoring, IEEE Aerospace Conference, doi:10.1109/AERO.2013.6497317, 2013.
Eckermann, S. D. and Preusse, P.: Global Measurements of Stratospheric Mountain Waves from Space, Science, 286, 1534–1537, doi:10.1126/science.286.5444.1534, 1999.
Ern, M., Preusse, P., Alexander, M. J., and Warner, C. D.: Absolute values of gravity wave momentum flux derived from satellite data, Journal of Geophysical Research, 109, D20 103, doi:10.1029/2004JD004752, 2004.
Faber, A., Llamedo, P., Schmidt, T., de la Torre, A., and Wickert, J.: On the determination of gravity wave momentum flux from GPS radio occultation data, Atmospheric Measurement Techniques, 6, 3169–3180, doi:10.5194/amt-6-3169-2013, 2013.
Fjeldbo, G., Kliore, A. J., and Eshlemen, V. R.: Neutral Atmosphere of Venus as studied with Mariner-V radio occultation experiments, The Astronomical Journal, 76, 123–140, doi:10.1086/111096, 1971.
Fritts, D. C. and Alexander, M. J.: Gravity wave dynamics and effects in the middle atmosphere, Reviews of Geophysics, 41, 1003, doi:10.1029/2001RG000106, 2003.
Geller, M., Alexander, M. J., Love, P., Bacmeister, J., Ern, M., Hertzog, A., Manzini, E., Preusse, P., Sato, K., Scaife, A., and Zhou, T.: A Comparison between Gravity Wave Momentum Fluxes in Observations and Climate Models, Journal of Climate, 26, 6383–6405, doi:10.1175/JCLI-D-12-00545.1, 2013.

Gong, J., Wu, D. L., and Eckermann, S. D.: Gravity wave variances and propagation derived from AIRS radiances, Atmospheric Chemistry and Physics, 12, 1701–1720, doi:10.5194/acp-12-1701-2012, 2012.

Harrower, M. and Brewer, C.: ColorBrewer.org: An Online Tool for Selecting Colour Schemes for Maps, The Cartographic Journal, 40, 27–37, doi:10.1179/000870403235002042, 2003.

Hei, H., Tsuda, T., and Hirooka, T.: Characteristics of atmospheric gravity wave activity in the polar regions revealed by GPS radio occultation data with CHAMP, Journal of Geophysical Research, 113, D04 107, doi:10.1029/2007JD008938, 2008.

Hendricks, E., Doyle, J., Eckermann, S. D., Jiang, Q., and Reinecke, P.: What Is the Source of the Stratospheric Gravity Wave Belt in Austral Winter?, Journal of the Atmospheric Sciences, 71, 1583–1592, doi:10.1175/JAS-D-13-0332.1, 2014.

Hertzog, A., Boccara, G., Vincent, R. A., Vial, F., and Cocquerez, P.: Estimation of gravity wave momentum flux and phase speeds from quasi-Lagrangian stratospheric balloon flights. Part II: Results from the Vorcore campaign in Antarctica., Journal of the Atmospheric Sciences, 65, 3056–3070, doi:10.1175/2008JAS2710.1, 2008.

Hertzog, A., Alexander, M. J., and Plougonven, R.: On the Intermittency of Gravity Wave Momentum Flux in the Stratosphere, Journal of the Atmospheric Sciences, 69, 3433–3448, doi:10.1175/JAS-D-12-09.1, 2012.

Hoffmann, L., Xue, X., and Alexander, M. J.: A global view of stratospheric gravity wave hotspots located with Atmospheric Infrared Sounder observations, Journal of Geophysical Research: Atmospheres, 118, 416–434, doi:10.1029/2012JD018658, 2013.

Hoskins, B. and Hodges, K.: A new perspective on Southern Hemisphere storm tracks, Journal of Climate, 18, 4108–4129, doi:10.1175/JCLI3570.1, 2005.

Kursinski, E. R., Hajj, G. A., Schofield, J. T., Linfield, R. P., and Hardy, K. R.: Observing Earth's atmosphere with radio occultation measurements using the Global Positioning System, Journal of Geophysical Research, 102, 23 429–23 465, doi:10.1029/97JD01569, 1997.

Liou, Y. A., Pavelyev, A. G., Pavelyev, A. A., Yen, N., Huang, C. Y., and Fong, C. J.: FORMOSAT-3/COSMIC GPS radio occultation mission: Preliminary results, IEEE Transactions on Geoscience and Remote Sensing, 45, 3813–3826, 2007.

Marquardt, C. and Healy, S.: Measurement noise and stratospheric gravity wave characteristics obtained from GPS occultation data, Journal of the Meteorological Society of Japan, 83, 417–428, doi:10.2151/JMSJ-83-417, 2005.

McDonald, A. J.: Gravity wave occurrence statistics derived from paired COSMIC/FORMOSAT3 observations, Journal of Geophysical Research, 117, D15 106, doi:10.1029/2011JD016715, 2012.

McLandress, C., Shepherd, T. G., Polavarapu, S., and Beagley, S. R.: Is Missing Orographic Gravity Wave Drag near 60°S the Cause of the Stratospheric Zonal Wind Biases in Chemistry–Climate Models?, Journal of the Atmospheric Sciences, 69, 802–818, doi:10.1175/JAS-D-11-0159.1, 2012.

O'Sullivan, D. and Dunkerton, T. J.: Generation of inertia-gravity waves in a simulated life-cycle of baroclinic instability, Journal of the Atmospheric Sciences, 52, 3695–3716, doi:10.1175/1520-0469(1995)052<3695:GOIWIA>2.0.CO;2, 1995.

Plougonven, R., Hertzog, A., and Guez, L.: Gravity waves over Antarctica and the Southern Ocean: consistent momentum fluxes in mesoscale simulations and stratospheric balloon observations, Quarterly Journal of the Royal Meteorological Society, 139, 101–118, doi:10.1002/qj.1965, 2013.

Preusse, P., Doernbrack, A., and Eckermann, S.: Space-based measurements of stratospheric mountain waves by CRISTA 1. Sensitivity, analysis method, and a case study, Journal of Geophysical Research, 107, 8178, doi:10.1029/2001JD000699, 2002.

Preusse, P., Eckermann, S. D., and Ern, M.: Transparency of the atmosphere to short horizontal wavelength gravity waves, Journal of Geophysical Research, 113, D24 104, doi:10.1029/2007JD009682, 2008.

Preusse, P., Schroeder, S., Hoffmann, L., Ern, M., Friedl-Vallon, F., Ungermann, J., Oelhaf, H., Fischer, H., and Riese, M.: New perspectives on gravity wave remote sensing by spaceborne infrared limb imaging, Atmospheric Measurement Techniques, 2, 299–311, doi:10.5194/amt-2-299-2009, 2009.

Preusse, P., Ern, M., Bechtold, P., Eckermann, S. D., Kalisch, S., Trinh, Q. T., and Riese, M.: Characteristics of gravity waves resolved by ECMWF, Atmospheric Chemistry and Physics, 14, doi:10.5194/acp-14-10483-2014, 2014.

Sato, K., Watanabe, S., Kawatani, Y., Tomikawa, Y., Miyazaki, K., and Takahashi, M.: On the origins of mesospheric gravity waves, Geophysical Research Letters, 36, L19 801, doi:10.1029/2009GL039908, 2009.

Sato, K., Tateno, S., Watanabe, S., and Kawatani, Y.: Gravity Wave Characteristics in the Southern Hemisphere Revealed by a High-Resolution Middle-Atmosphere General Circulation Model., Journal of the Atmospheric Sciences, 69, 1378–1396, doi:10.1175/JAS-D-11-0101.1, 2012.

Savitzky, A. and Golay, M. J. E.: Smoothing and Differentiation of Data by Simplified Least Squares Procedures, Analytical Chemistry, 36, 1627–1639, 1964.

Scaife, A., Butchart, N., Warner, C., Stainforth, D., Norton, W., and Austin, J.: Realistic quasi-biennial oscillations in a simulation of the global climate, Geophysical Research Letters, 27, 3481–3484, doi:10.1029/2000GL011625, 2000.

Stockwell, R., Mansinha, L., and Lowe, R. P.: Localization of the complex spectrum: the S-Transform, IEEE Transactions on Signal Processing, 44, 998–1001, 1996.

Tsuda, T., Lin, X., Hayashi, H., and Noersomadi: Analysis of vertical wave number spectrum of atmospheric gravity waves in the stratosphere using COSMIC GPS radio occultation data, Atmospheric Measurement Techniques, 4, 1627–1636, doi:10.5194/amt-4-1627-2011, 2011.

Wang, L. and Alexander, M. J.: Global estimates of gravity wave parameters from GPS radio occultation temperature data, Journal of Geophysical Research, 115, D21 122, doi:10.1029/2010JD013860, 2010.

Watanabe, S., Kawatani, Y., Tomikawa, Y., Miyazaki, K., Takahashi, M., and Sato, K.: General aspects of a T213L256 middle atmosphere general circulation model, Journal of Geophysical Research, 113, D12 110, doi:10.1029/2008JD010026, 2008.

Wright, C. J. and Gille, J. C.: HIRDLS observations of gravity wave momentum fluxes over the monsoon regions, Journal of Geophysical Research, 116, doi:10.1029/2011JD015725, 2011.

Wright, C. J. and Gille, J. C.: Detecting overlapping gravity waves using the S-Transform, Geophysical Research Letters, 40, 1850–1855, doi:10.1002/grl.50378, 2013.

Wright, C. J., Osprey, S. M., and Gille, J. C.: Global observations of gravity wave intermittency and its impact on the observed momentum flux morphology, Journal of Geophysical Research: Atmospheres, 118, 10,980–10,993, doi:10.1002/jgrd.50869, 2013.

Wright, C. J., Osprey, S. M., and Gille, J. C.: Global distributions of overlapping gravity waves in HIRDLS data, Atmospheric Chemistry and Physics Discussions, pp. 4333–4382, doi:10.5194/acpd-15-4333-2015, 2015.

Wu, D. L. and Jiang, J. H.: MLS observations of atmospheric gravity waves over Antarctica, Journal of Geophysical Research, 107, 4773, doi:10.1029/2002JD002390, 2002.

Wu, D. L. and Waters, J. W.: Satellite observations of atmospheric variances: A possible indication of gravity waves, Geophysical Research Letters, 23, 3631–3634, doi:10.1029/96GL02907, 1996.

Yan, X., Arnold, N., and Remedios, J.: Global observations of gravity waves from High Resolution Dynamics Limb Sounder temperature measurements: A year-long record of temperature amplitude, Journal of Geophysical Research, 115, D10 113, doi:10.1029/2008JD011511, 2010.

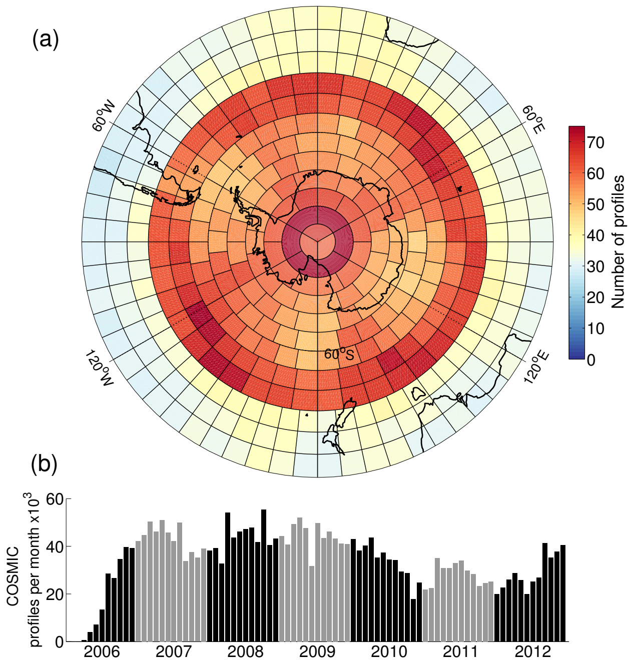

Figure 1. Polar stereographic projection of monthly-mean COSMIC sampling density for the period 2007-2012 (a), and total number of occultations per month for the period 2006-2012 (b). Each box in (a) represents an equal area of approximately 550 km^2. Alternating years in (b) are shown by black and gray bars.

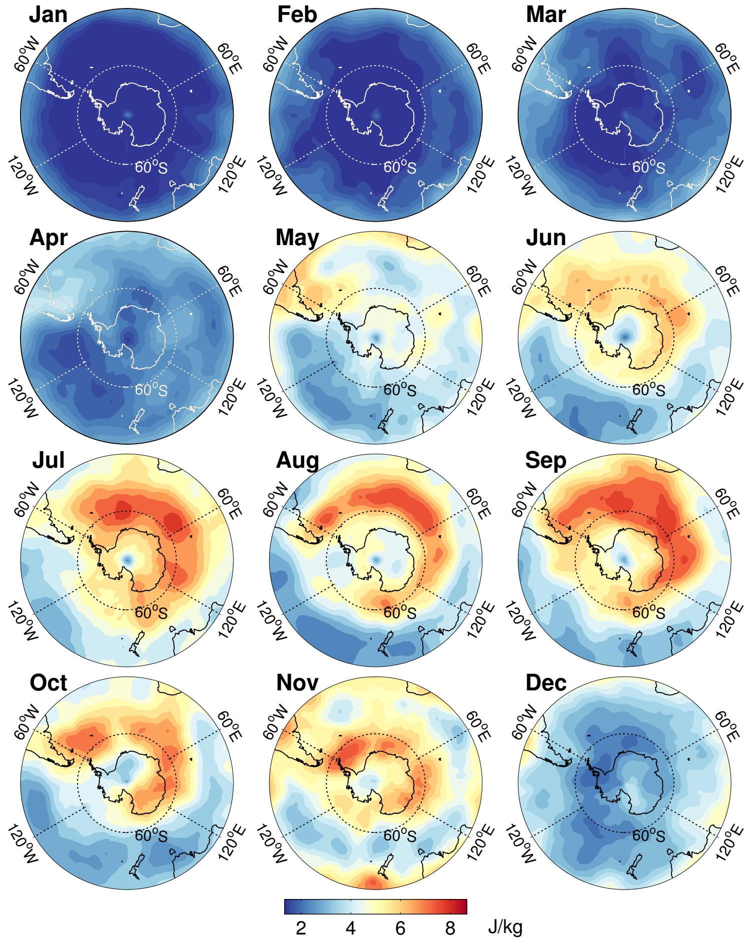

Figure 2. Polar stereo projections of monthly-mean potential energy per unit mass E_p in the southern hemisphere averaged over the height range 26-36 km (∼20-5 hPa) for each month in 2010.

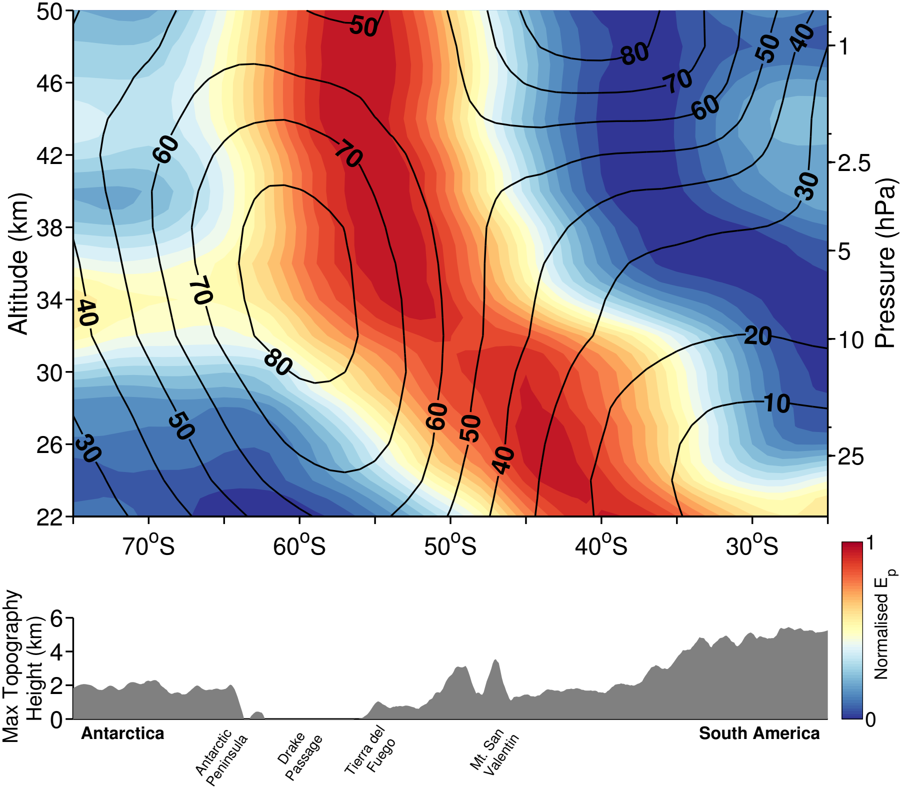

Figure 3. Normalised monthly-mean meridional cross-section of E_p in August 2010 over the southern Andes and Antarctic Peninsula (top panel) and maximum topography height (bottom panel) in a $\pm 5°$ slice centred on 65° W. Monthly-mean zonal-mean winds from ECMWF operational analyses are shown by thick contours in the top panel, at intervals of 10 m/s. Note the E_p has been normalised at each height level to highlight the vertical structure.

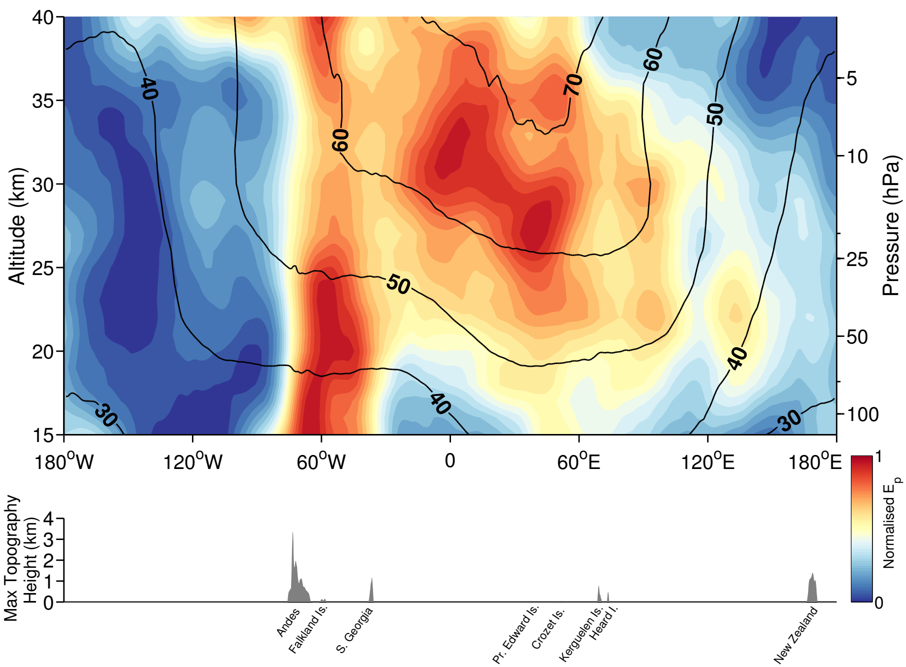

Figure 4. Normalised monthly mean zonal cross-section of E_p for August 2010 over Southern Ocean (top panel) and maximum topography height (bottom panel) in a $\pm10°$ slice centred on 50° S. Monthly mean zonal mean winds from ECMWF operational analyses are shown by thick contours in the top panel, at intervals of 10 m/s. Note the E_p has been normalised at each height level to highlight the vertical structure.

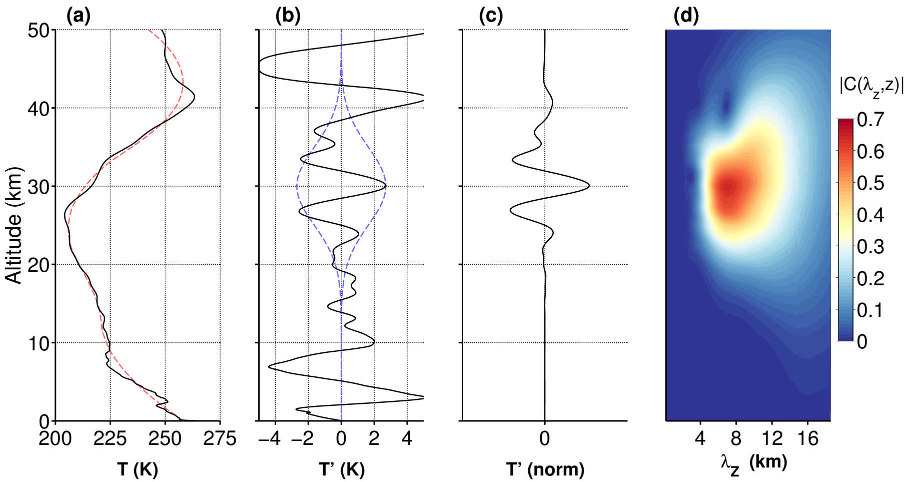

Figure 5. Wave identification (Wave-ID) methodology for an example COSMIC profile at 2319 UTC on 1st August 2010 at 53° S, 50° W. Panels show (a) raw temperature profile T (black solid) and filtered background temperature profile $\bar{T}$ (red dashed), (b) Temperature perturbation profile T' (black solid) and a Gaussian window centred on 30 km (blue dashed), (c) windowed, RSS normalised and zero-averaged perturbation profile T'_{norm}, (d) magnitudes of the spectral coefficients of the Continuous Wavelet Transform of T'_{norm}. For details, see text.

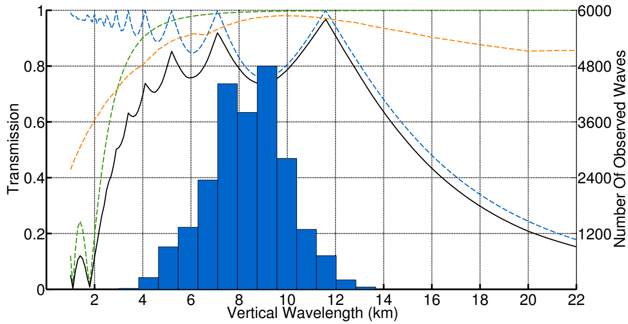

Figure 6. Transmission against vertical wavelength for each step in our Wave-ID processing for synthetic waves with λ_Z < 22 km centred at 30 km altitude: background subtraction (blue dashed); noise reduction (green dashed); Gaussian windowing and CWT (orange dashed); and the combined transmission (black solid). Blue bars show a histogram (right axis) of number of waves identified in COSMIC data in the region 35-75°S 0-90°W during June-August 2006-2012 using this method.

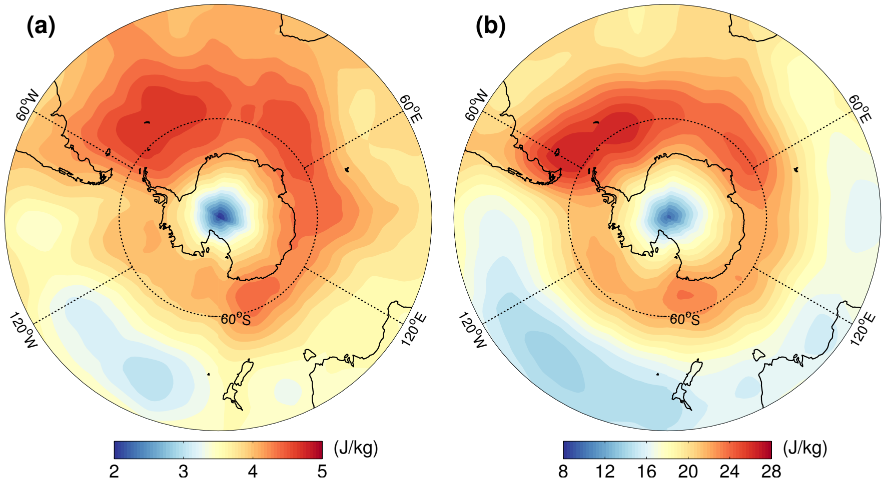

Figure 7. Polar stereo projections of E_p at 30 km ($\sim$10 hPa) for June-August 2006-2012 using (a) all available COSMIC profiles and (b) only individually identified waves using the Wave-ID method (see text).

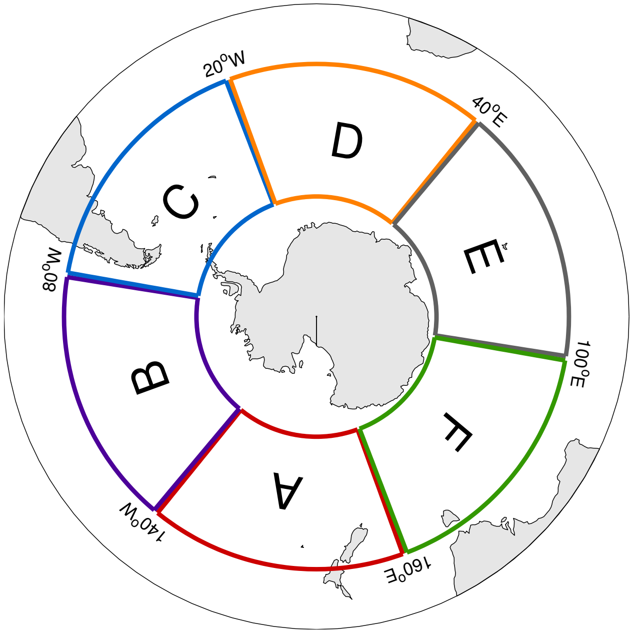

Figure 8. Polar stereo projection showing longitudinal Sectors A-F in the latitude band 40-65°S used in Figure 9.

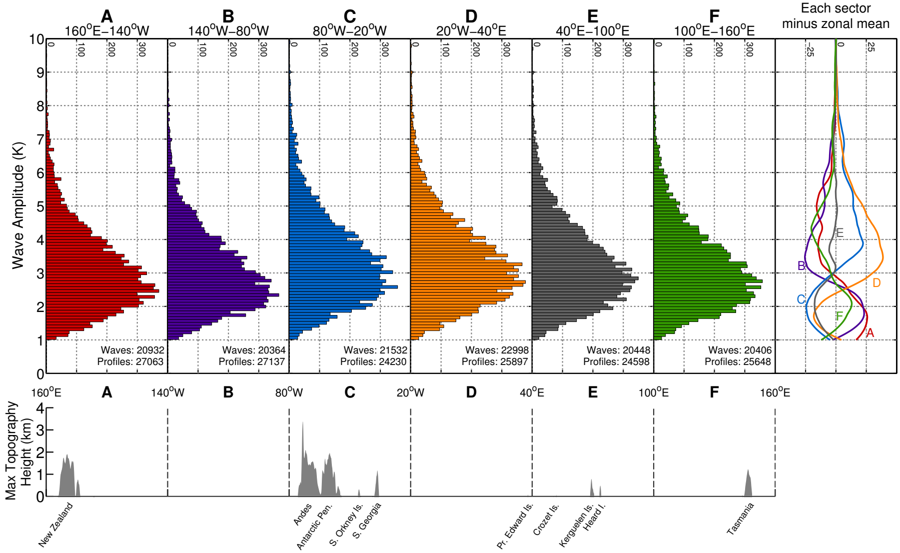

Figure 9. Histograms of individual wave amplitudes detected during June-August 2006-2012 in longitudinal sectors A-F in the latitude band 40-65°S using the Wave-ID method (see text). The right-most panel shows the difference between the wave amplitude distribution in each sector and the zonal-mean distribution. The bottom panel shows maximum topography height in the latitude band 40-65°S

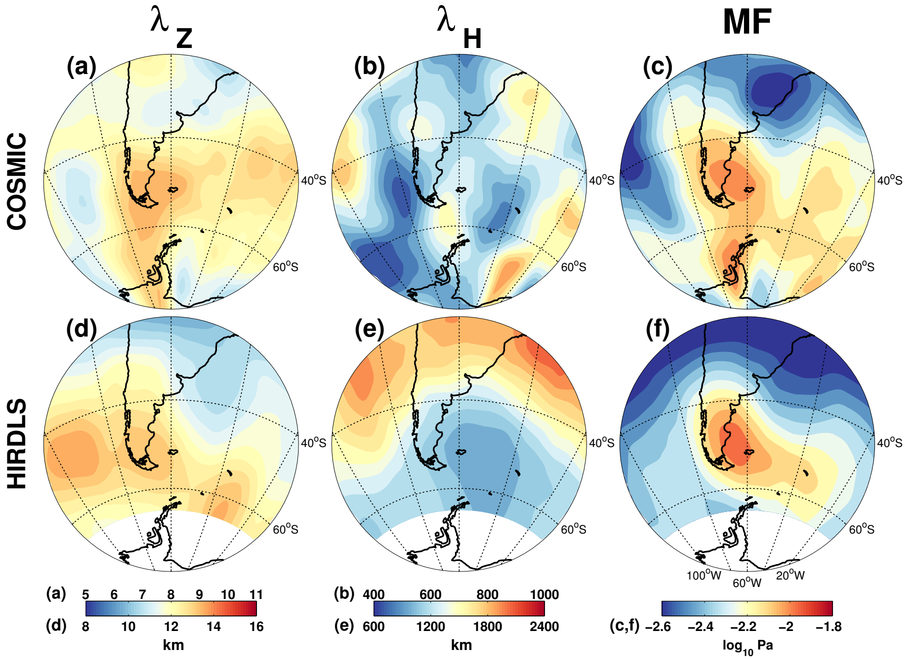

Figure 10. Orthographic projections of vertical wavelength λ_Z, horizontal wavelength λ_H and momentum flux (MF) for COSMIC (a,b,c) and HIRDLS (d,e,f) at 30 km (~10 hPa) during June-August 2006.

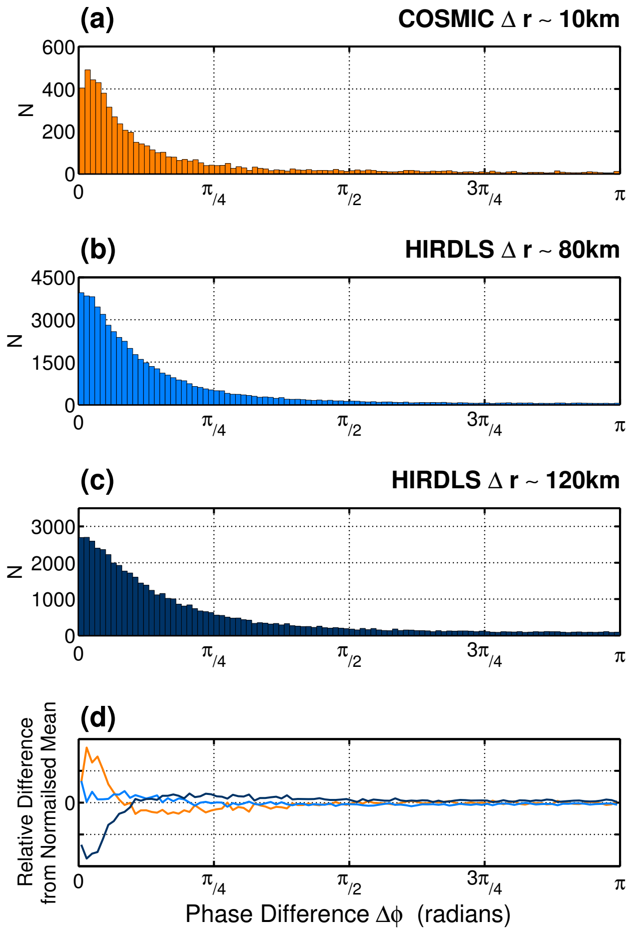
(a)
COSMIC Δ r ~ 10km
600
400
200
0
N
0
π/4
π/2
3π/4
π
(b)
HIRDLS Δ r ~ 80km
4500
3000
1500
0
N
(c)
HIRDLS Δ r ~ 120km
3000
2000
1000
0
N
(d)
Relative Difference from Normailsed Mean
Phase Difference Δϕ (radians)

Figure 11. Histograms of gravity wave phase difference $\Delta\phi$ in (a) COSMIC profile-pairs, (b) HIRDLS "downscan-upscan" profile-pairs and (c) HIRDLS "upscan-downscan" profile-pairs globally during JJA 2006. Bottom panel (d) shows normalised relative difference of COSMIC (orange), HIRDLS downscan-upscan (light blue) and HIRDLS upscan-downscan (dark blue) from the mean of all three.

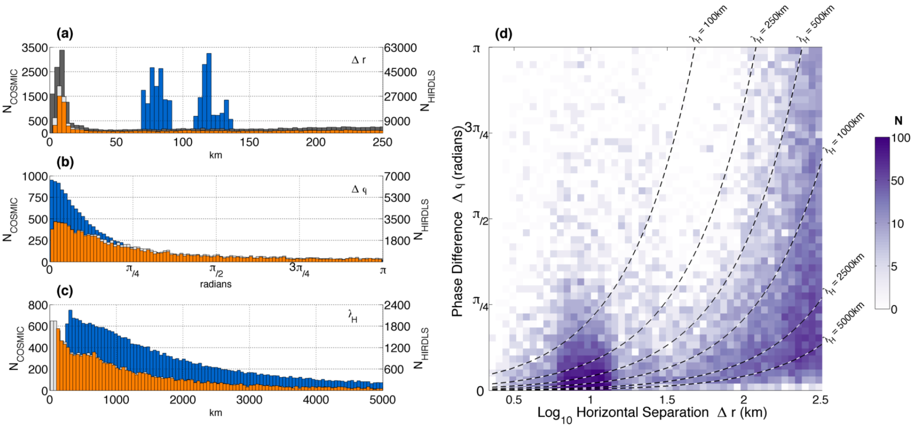

Figure 12. Number of COSMIC (N_{COSMIC}, orange and grey bars) and HIRDLS (N_{HIRDLS}, blue bars) profile-pairs against (a) horizontal separation Δr (b) phase difference $\Delta\phi$ and (c) projected horizontal wavelength λ_H globally for June-August 2006. Dark grey bars in (a) correspond to all available COSMIC profile-pairs. Light grey bars in (a,b,c) correspond to COSMIC profile-pairs in which a coherent wave was identified via the Wave-ID method. Orange bars in (a,b,c) correspond to COSMIC profile-pairs in which a wave was identified with $100 < \lambda_H < 5000$ km. Panel (d) shows a density plot of number of COSMIC profile-pairs N against horizontal separation and phase difference. Dashed black lines of constant λ_H are found via the relation in Eqn. 9.